

Review

# Air Cathodes and Bifunctional Oxygen Electrocatalysts for Aqueous Metal–Air Batteries

Jadranka Milikić <sup>1,\*</sup>, Ana Nastasić <sup>1</sup>, Marta Martins <sup>2</sup>, César A. C. Sequeira <sup>2</sup> and Biljana Šljukić <sup>1,2</sup>

<sup>1</sup> Faculty of Physical Chemistry, University of Belgrade, 11158 Belgrade, Serbia; 20190005@student.ffh.bg.ac.rs (A.N.); biljka@ffh.bg.ac.rs (B.Š.)

<sup>2</sup> Center of Physics and Engineering of Advanced Materials, Laboratory for Physics of Materials and Emerging Technologies, Chemical Engineering Department, Instituto Superior Técnico, Universidade de Lisboa, 1049-001 Lisbon, Portugal; marta.oliveira.martins@tecnico.ulisboa.pt (M.M.); cesarsequeira@tecnico.ulisboa.pt (C.A.C.S.)

\* Correspondence: jadranka@ffh.bg.ac.rs

**Abstract:** One of the most popular solutions for electrochemical energy storage is metal–air batteries, which could be employed in electric vehicles or grid energy storage. Metal–air batteries have a higher theoretical energy density than lithium-ion batteries. The crucial components for the best performance of batteries are the air cathode electrocatalysts and corresponding electrolytes. Herein, we present several of the latest studies on electrocatalysts for air cathodes and bifunctional oxygen electrocatalysts for aqueous zinc–air and aluminium–air batteries.

**Keywords:** metal–air batteries; oxygen evolution reaction; oxygen reduction reaction; bifunctional electrocatalyst; zin–air batteries; aluminium–air batteries

## 1. Introduction



**Citation:** Milikić, J.; Nastasić, A.; Martins, M.; Sequeira, C.A.C.; Šljukić, B. Air Cathodes and Bifunctional Oxygen Electrocatalysts for Aqueous Metal–Air Batteries. *Batteries* **2023**, *9*, 394. <https://doi.org/10.3390/batteries9080394>

Academic Editor: Jun Liu

Received: 9 June 2023

Revised: 7 July 2023

Accepted: 25 July 2023

Published: 28 July 2023



**Copyright:** © 2023 by the authors. Licensee MDPI, Basel, Switzerland. This article is an open access article distributed under the terms and conditions of the Creative Commons Attribution (CC BY) license (<https://creativecommons.org/licenses/by/4.0/>).

In recent years, human society has been facing the consequences of using fossil fuels as the primary energy source and reduced energy supplies due to the exponential increase in energy demand. Consequently, renewable energy sources, such as solar, wind, and water power, have accounted for increasing energy use. These energy resources have a highly fluctuating and sporadic power output. Therefore, the parallel use of electrochemical energy conversion and storage technologies, including capacitors, supercapacitors, batteries, and fuel cells, is necessary. Such technologies enable the easy and efficient use of the aforementioned sustainable energy sources by storing the produced electricity, which can be used later [1]. Energy is stored electrostatically in capacitors, while in supercapacitors, energy is stored both electrostatically and electrochemically. Both batteries and fuel cells transform chemical energy into electricity. The main difference is that fuel cells are an open system, where the electrodes are constantly supplied with fuel, and there is no need for charging. Conversely, batteries are a closed system involving the internal consumption of reactants and require charging [1]. Batteries are divided into two groups: primary batteries (non-rechargeable) and secondary batteries (rechargeable). Secondary batteries, e.g., lithium (Li)-ion, nickel–cadmium, and zinc (Zn)–air batteries, can be charged multiple times. The rechargeable nature of secondary batteries is based on a reversible redox reaction that can proceed in both directions. Secondary batteries have a very high energy efficiency of 75% [1]. Other advantages of batteries include their high energy density, long life, and availability in different sizes. The most commercialised batteries are lithium-ion batteries, which, unfortunately, are approaching their performance upper limit [2,3]. Therefore, researchers are actively working on developments in electrochemical energy storage and conversion and are looking for a solution to the energy supply problem beyond lithium-ion batteries. Metal–air batteries (MABs) are investigated as a possible solution due to their low production cost, high specific energy, power density, and safety [1].

Research related to MABs began prior to lithium-ion batteries, as early as 1878, when Maiche designed the first primary Zn–air battery. This type of battery became commercially available on the market in 1932 [2]. During the 1960s, aqueous iron (Fe)–, aluminum (Al)–, and magnesium (Mg)–air batteries were established, and a few decades later, non-aqueous Li–air, sodium (Na)–air, and potassium (K)–air batteries [1]. Despite their early beginnings, their development has been significantly slowed by problems associated with their components. A rechargeable solid-state Li–O<sub>2</sub> battery was first introduced in 1996 by Abraham et al. when they successfully demonstrated three charge–discharge cycles [4]. At the time of their first appearance, Li–air batteries did not attract significant attention from the research community. In 2006, the Bruce group reconsidered Li–air batteries and presented their good electrochemical performance through the prism of practical applications. In the future, driving distances of slightly over 550 km are forecast for Li–air batteries [4]. As there are very limited Li reserves on Earth, the Na–air battery was introduced in 2011 as a promising alternative to Li–air batteries due to the similar chemical characteristics of Li and Na [4]. The most commonly used electrolyte in Li–air batteries is non-aqueous due to the violent reaction of Li with water. Still, in 2008, a water-stable Li metal anode with a water-stable Li-conducting glass ceramic and a Li-conducting polymer electrolyte was presented for the first time as the anode for Li–air batteries with the aqueous LiCl catholyte [5].

Similarly, in 2013, a mixed aqueous (NaOH)/aprotic electrolyte obtained through a ceramics separator was introduced for Na–air batteries [5]. Iron and zinc as MAB anodes have attracted attention primarily for applications in electric vehicles due to their abundance and low cost. Despite all the setbacks, the development of MABs has followed the evolution of materials science; thus, in 2015, a metal-free bifunctional cathode electrocatalyst for Zn–air batteries was presented [1]. Also, the development of MABs has followed the market demands for flexible batteries; thus, in 2015, a gel polymer electrolyte for flexible Zn–air batteries was presented [1]. Zn–air and Al–air batteries are considered ideal for application in flexible batteries due to their low cost, safety, and high energy density [6]. The Al–air battery was introduced in 1962 by Zaromb et al. Since then, efforts have been focused on making them usable in various systems, such as electric vehicles, military communication, and unmanned aircraft.

Consequently, in 2016, researchers confirmed that an electric vehicle can reach a travel distance of over 3000 km using an Al–air battery weighing 100 kg [1]. Mg–air batteries, which are generally primary, have received less attention from researchers, but they have found applications primarily in systems with limited space for battery implementation. They are used in small, lightweight, portable devices for civil and military applications [1]. The second most abundant element in the Earth's crust and a semiconductor successfully used in electronics, silicon (Si), was first used as an anode in MABs in 2009 by G. Cohn et al. [7]. Doped Si was used as the anode to improve electronic conductivity. Although the first Si–air battery was fabricated using a non-aqueous electrolyte, today there are aspirations to develop Si–air batteries with an aqueous alkaline electrolyte such as KOH [1]. Recently, special attention has been paid to research related to MABs, and the number of publications on MABs has increased more than 15 times since 2011 [3].

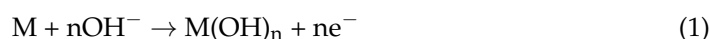
MABs comprise four main components—a porous air cathode, a metal anode, an electrolyte, and a suitable separator that mechanically separates the anode and cathode. MABs are continuously supplied with oxygen from the atmosphere at the cathode and are therefore considered a hybrid of a battery and a fuel cell [2]. MABs have high theoretical specific energy density values ranging from 1.2 to 11.4 kWh kg<sup>-1</sup> [2], i.e., ca. 3–30 times higher than the theoretical specific energy density value of lithium-ion batteries, one of the most commercialised batteries today [2]. The theoretical specific capacities of different MABs range from 0.68 to 3.86 Ah g<sup>-1</sup> [8], making lithium–air batteries (3.86 Ah g<sup>-1</sup>) and aluminium–air batteries (2.98 Ah g<sup>-1</sup>) some of the most promising candidates for solving the energy supply problem among non-aqueous and aqueous MABs, respectively. Alkali

(e.g., Li and K); earth-abundant (e.g., Al and Si); alkaline earth (e.g., Mg and Ca); or first-row transition metals (e.g., Zn) are employed as MAB anodes [3].

Electrolytes used in MABs can be divided into four groups: aqueous (protic), non-aqueous (aprotic), hybrid, and solid-state electrolytes. MABs based on alkaline anodes are stable in non-aqueous electrolytes. In contrast, anodes made of other metals, e.g., Mg, Fe, Al, and Zn, are stable in aqueous media but equipped with a hydrophobic layer that has a protective function and prevents electrolyte leakage [1]. In contrast to non-aqueous electrolytes, aqueous electrolytes have advantages such as high safety, a high ionic conductivity of about  $1\text{ S cm}^{-1}$ , non-toxicity, and a low cost [3]. Therefore, the flammability of some organic solvents, their possible polluting influence, their low conductivity of about  $1\text{--}10\text{ mS cm}^{-1}$ , and their high production cost prevent the wider application of non-aqueous MABs [3].

The separator prevents electronic contact between the anode and cathode, as well as the mixing of the anolyte and catholyte, but also allows ion exchange to complete the circuit; therefore, separators are porous polymeric membranes [9,10]. In commercial cells, the separator is usually a polypropylene membrane with a porosity of  $10\text{--}20\text{ }\mu\text{m}$  [9].

Metals such as Zn, Al, Mg, and Fe are thermodynamically unstable in an aqueous environment; however, coating their surface with corresponding hydroxides or oxides under certain conditions makes them more stable in aqueous electrolytes and, therefore, more suitable for use in aqueous MABs. Scheme 1 illustrates the working principle of aqueous MABs. During discharge, the metal (M) is oxidised at the anode to release n electrons (n is the oxidation number of the metal) and metal ions that combine with hydroxide ions to form metal hydroxide (Equation (1)) [3]. The released electrons are transported through the external circuit to the cathode, where they take part in the oxygen reduction reaction (ORR) together with water and oxygen molecules from the atmosphere to produce hydroxide ions, which are further transported through the separator to the anode to complete the circuit (Equation (2)) [3].



The overall reaction is obtained by combining Equations (1) and (2) (Equation (3)) [3]:

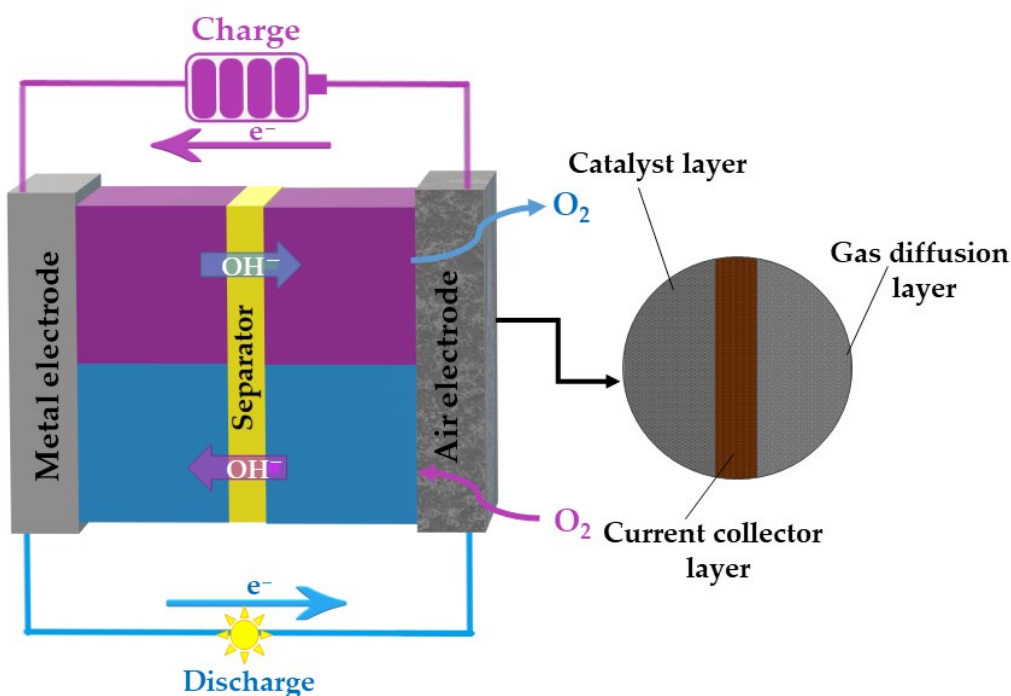


During battery charging, the above reactions occur in the opposite direction [3].

Zinc ions in aqueous electrolytes can be directly reduced, while MABs employing other metals must be charged mechanically by charging their metal anode [3].

Alkali metals are very reactive in aqueous solutions, so MABs with anodes based on Li, Na, or K use aprotic electrolytes. It is important to point out that the ORR in aprotic media has a completely different mechanism than in aqueous electrolytes. Non-aqueous MABs are still at the beginning of their development due to the serious challenges they face, including the abovementioned problems with aprotic electrolytes and a completely different mechanism for the ORR [11–14].

Although alkaline electrolytes (e.g., KOH) cause the corrosion of anode materials, rapid carbonisation, and the formation of dendrites on the metal, they are often used as electrolytes for air cathodes. These electrolytes facilitate kinetics of the oxygen evolution reaction (OER) and ORR in contrast to neutral electrolytes, which are somewhat milder and more environmentally friendly but have sluggish OER/ORR kinetics [15].



**Scheme 1.** The working principle of aqueous MABs (left) and air cathode construction (right).

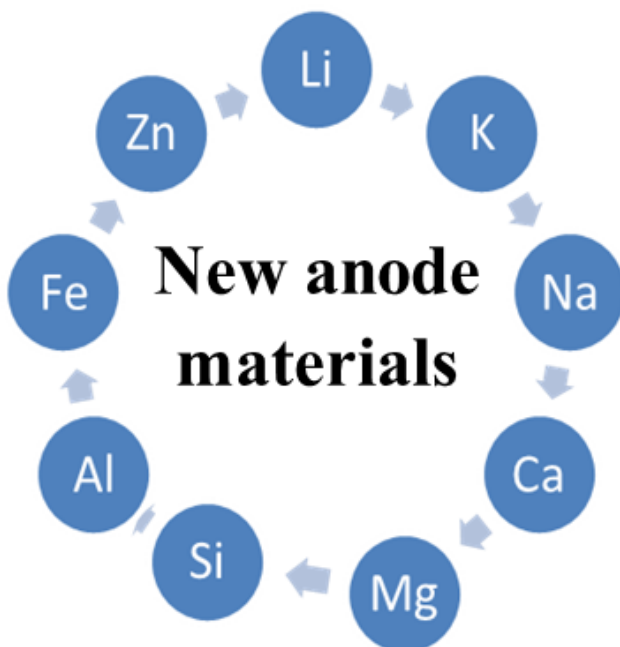
The air cathode is one of the key components of MABs, and its properties are crucial for their performance. An efficient air electrode should allow the rapid diffusion of oxygen and the fast migration of  $OH^-$ , prevent water permeation, have good activity for the ORR in primary MABs or both the ORR and OER in secondary MABs, and present physical and electrochemical stability in an alkaline environment and at high potentials [3]. No air electrode fulfils all these requirements at the same time. A conventional air electrode is constructed from three components: an electrocatalyst, a gas diffusion layer, and a current collector placed between these two components to enable the transfer of electrons from or to the catalyst layer (Scheme 1) [3]. All three of these layers are porous to maximise oxygen diffusion [3]. During the ORR, oxygen from the air diffuses from the porous, thin, and (to a certain extent) hydrophobic gas diffusion layer through the current collector layer to the catalyst layer. Simultaneously, electrons from the metal anode pass through the current collector to the catalyst layer and combine with oxygen molecules at the catalyst's sites. For the OER, the oxygen and electron pathways are inverse [3]. The current collector layer should be sufficiently conductive and tough, given that its role is primarily to collect electrons and provide physical support, i.e., prevent tearing [3]. The catalyst layer is where the OER and ORR occur; therefore, it is the component that most strongly affects the efficiency and durability of MABs. As different reactions occur on the electrodes during the charging and discharging of the battery, some catalysts are intended for only one of these reactions, while some have bifunctional catalytic activity.

Although a lot of work has been carried out in the field of MABs, challenges related to the metal anode (passivation, corrosion, and dendritic formation); electrolyte ( $CO_2$  dissolution from the air, the absorption of moisture, and the evaporation of the electrolyte) [15]; air cathode (sluggish OER/ORR kinetics and poor cycling stability) [2]; and the choice of a suitable separator significantly reduce their effectiveness and therefore prevent the commercialisation of MABs and the utilisation of their full potential. The current possible solutions to most of these problems lead to an increase in the price and size of batteries and a decrease in energy density [2]. Therefore, it is extremely important to continue research in this field.

This review focuses on aqueous MABs, emphasising new advances in materials to be employed as electrocatalysts for the OER and ORR, as well as the mechanism of the aforementioned reactions in alkaline media.

## 2. Anode Materials for MABs

As mentioned, MABs are electrochemical cells wherein the metal is oxidised and oxygen is reduced. These devices feature a high energy density, ca. 3–30 times higher than commercial lithium-ion batteries [2,16]. Zinc, aluminium, and magnesium alloys are considered especially advantageous for some applications because they are inexpensive and lightweight. Lithium, sodium, and potassium are stable in non-aqueous environments, while magnesium, aluminium, iron, and zinc are stable in aqueous systems (Scheme 2) [2,16]. Concerning the abundance of these metals, lithium is not considered an abundant element despite being distributed in the lithosphere. In contrast, Na is one of the most abundant elements and it is second lightest and smallest metal after Li. [4].



**Scheme 2.** Most relevant anode materials for metal–air batteries.

Li–air batteries are the most studied systems due to their specific energy of ca.  $3458 \text{ Wh kg}^{-1}$  (Table 1), which is higher than that of common lithium-ion batteries ( $270 \text{ Wh kg}^{-1}$ ) and other rechargeable systems such as lithium–sulfur batteries ( $2600 \text{ Wh kg}^{-1}$ ) [17]. Nevertheless, obtaining rechargeable Li–air batteries is difficult. Li anodes have some drawbacks, including lithium dendrites and the solid electrolyte formation during cycling [18]. It has been reported that Li metal can be restored only partially in battery cycling with the continuous deposition of lithium hydroxide on the anode surface for the discharge/charge process in a non-aqueous solution [17]. The formation of LiOH can be attributed to the degradation in the discharge/charge process. Using a protective layer can help prevent the corrosion of the lithium anode in aqueous and non-aqueous electrolytes when there is moisture.

Zn metal gained the research community's attention as an anode material in MABs to overcome the high reactivity of lithium in aqueous media [3]. Zn–air batteries are characterised by an exceptional energy density ( $1218 \text{ Wh Kg}^{-1}$ ), which makes them favourable for mobile and other electronic applications (Table 1). Furthermore, they have advantages such as the abundant availability of their components along with their inexpensive and safe manufacturing process, long shelf-life, and flat discharge voltage [3]. Rechargeable Zn–air batteries are classified into two types: mechanically and electrically rechargeable batteries. The former are recharged by introducing fresh Zn electrodes to avoid the poor reversibility

of Zn. The excessive cost of the Zn recharging chain and distribution limits this option. In electrically rechargeable Zn–air batteries, flowing media are used to improve the stability of the zinc electrode. However, the corrosion of air electrodes in the charging process affected the further development of Zn–air batteries at the end of the 20th century [19].

Moreover, Zn is considered a good alloy element for the anode in an aluminium–air device to ensure an increase in the nominal voltage and a decrease in the self-corrosion capacity. Still, studies performed on aluminium–zinc anodes have revealed a decrease in their discharge process due to Zn oxidation film formation. Thus, indium (In) was introduced into an Al-Zn anode, showing an improvement in the discharge of Al-air batteries by decreasing the resistance of the Zn oxidation film.

The Al-air battery is recognised for its high specific energy (Table 1), light weight, good recycling capability, environmental friendliness, and low price. Additionally, different electrolytes can be used: alkaline, saline, and non-aqueous [20]. The Al-air battery has a remarkable specific energy ( $8100 \text{ Wh kg}^{-1}$ , higher than that of Zn anodes) and a high theoretical voltage (2.7 V) [3,20]. Al is a readily available metal that can be recycled in substantial amounts [3].

The sodium–air battery has also been reported to have a high specific density ( $1600 \text{ Wh kg}^{-1}$ ) and capacity (Table 1). It should be mentioned that Na is among the most abundant elements on Earth (the sixth most abundant element). Moreover, it is less susceptible to decomposition during the charge/discharge of Na–air batteries as it combines with oxygen to form a more stable sodium superoxide ( $\text{NaO}_2$ ) [21].

Magnesium–air batteries bring the benefits of Mg's high abundance, high reaction activity, light weight, low toxicity, and relatively high safety. One of the main advantages of the magnesium–air battery is its capacity to be re-used by mechanically changing the magnesium anode and media. In the discharge process, the magnesium is oxidised to  $\text{Mg}^{2+}$ , releasing  $2 \text{ e}^-$ . Simultaneously, the  $\text{O}_2$  flowing in the air cathode is reduced to  $\text{OH}^-$ . The theoretical voltage of the Mg–air battery is reported to be 3.1 V, and the specific energy is  $6800 \text{ Wh kg}^{-1}$  (Table 1) [1,22].

Iron–air batteries comprise an Fe anode and a carbon–air cathode submerged in aqueous media at ambient temperature. The Fe oxidation and  $\text{O}_2$  reduction proceed during discharge and recharge from reverse reactions. The oxidation reaction of  $\text{Fe(OH)}_2$  to  $\text{FeOOH}$  or  $\text{Fe}_3\text{O}_4$  provides a higher specific energy ( $913 \text{ Wh kg}^{-1}$ ). Still, the formation of Fe(III) species is not desirable due to their higher stability and possible incomplete reduction during the recharge process. In the discharge process of an Fe–air battery, the  $\text{Fe(OH)}_2$  from the primary reaction of the anode deposits on the Fe electrode surface due to its low solubility in the alkaline electrolyte [1,23].

As mentioned above, silicon is the second most abundant element on Earth, and it has been widely studied in the semiconductor technology area in the last five-to-ten years. However, the exploration of Si as an anode material in batteries only started in 2009. Generally, silicon is oxidised at the anode for Si–air batteries in aqueous and non-aqueous media, and oxygen is reduced at the cathode. However, there are considerable differences depending on the solution [23].

Calcium is a highly abundant metal, >150% more abundant than sodium or magnesium. Its low molecular weight and  $E^\circ$  of  $-2.368 \text{ V}$  for  $\text{Ca}/\text{Ca}^{2+}$  redox in aqueous media make it an ideal contender for MAB anodes. Moreover, the deposition of Ca from aprotic solvents using salts such as  $\text{Ca}(\text{ClO}_4)_2$  or via alloy formation has recently been demonstrated.

Potassium has also attracted significant attention as an anode for MABs due to its low cell potential and considerable specific energy. Still, the reactivity of K induces side reactions with oxygen and water and the degradation of electrolyte solvents. Thus, this drastic reactivity of K metal restricts the choice of electrolyte. In addition, thick, porous solid–electrolyte interface layers are formed as a consequence of changes in the volume of K metal and surface side reactions during cycling. This further decreases the energy efficiency and reversibility of potassium–air batteries [20].

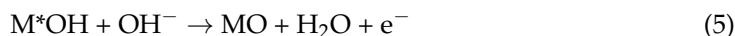
In summary, each metal has benefits and drawbacks as an anode electrode in MABs. The anode chemical activity defines the discharge capacity [6,24]. The reactions occurring are conditioned by the metal purity and the storage environment and can proceed under different conditions, influencing the battery efficiency. Table 1 shows the performance of MABs with different anode materials.

**Table 1.** Performance of MABs with different anode materials.

Anode Material	EOCV (V) vs. RHE	Durability	P <sub>max</sub> (mW cm <sup>-2</sup> )	Specific Energy (Wh Kg <sup>-1</sup> )	Ref.
Li	2.9	Up to 700 cycles	2	3458	[17]
Zn	1.7	500 h at −10 and 25 °C, 150 h at 40 °C under charging at 100 mA cm <sup>-2</sup>	10 to 435	1218	[25]
Al	2.7	Long	315	8100	[26]
Na	2.4	Holds 90% of its cell capacity after 300 cycles	39	1600	[26]
Mg	2.9	-	112.4	6800	[27]
Fe	1.3	More than 10,000 charge/ discharge cycles	-	913	[28]
Si	2.2	Short	0.3	8470	[29]
Ca	3.1	Long	-	250	[21,22]
K	-	Long	-	935	[30]

### 3. Mechanism of OER and ORR in Alkaline Media

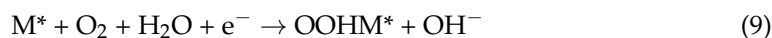
The OER mechanism in alkaline media presents a four-electron pathway ( $4\text{OH}^- \rightarrow \text{O}_2 + 2\text{H}_2\text{O} + 4\text{e}^-$ ) wherein, during the electron transfer between the active site of the metal electrocatalysts ( $\text{M}^*$ ) and  $\text{OH}^-$  ions, several intermediates such as  $\text{M}^*\text{OH}$ ,  $\text{M}^*\text{O}$ , and  $\text{M}^*\text{OOH}$  appeared [3,31–35], as described by the following equations (Equations (4)–(8)):



C. Feng et al. [32] explained that  $\text{O}_2$  can be formed in two ways. The first is given by Equations (4)–(6), finishing with the direct dissociation of  $\text{M}^*\text{O}$  to  $\text{M}^*$  and  $\text{O}_2$ , and the second is the reaction between  $\text{M}^*\text{O}$  and  $\text{OH}^-$  ions, forming an  $\text{M}^*\text{OOH}^-$  intermediate that then reacts with  $\text{OH}^-$  ions, forming  $\text{O}_2$ . That is, metal cations on the surface of the electrocatalyst are active sites for the OER, and their electrocatalytic activity directly depends on the  $\text{M}^*\text{-O}$  bond formed in the  $\text{M}^*\text{OH}$ ,  $\text{M}^*\text{O}$ , and  $\text{M}^*\text{OOH}$  intermediates [32]. B. Środa and coworkers [36] explained that OH groups have the lowest free energy, making them the most suitable for the OER. Thermodynamically and kinetically, the OER is energy-demanding and sluggish, because its mechanism requires the exchange of four electrons during the breaking and forming of four O-H and O-O bonds, respectively [37]. Aside from this, the most important part of the OER mechanism is the creation of O-O bonds, which has not been completely explained [37].

The ORR in alkaline media could occur by a two-electron ( $\text{O}_2 + 2\text{H}_2\text{O} + 2\text{e}^- \rightarrow \text{HO}_2^- + 4\text{OH}^-$ ) or four-electron ( $\text{O}_2 + 2\text{H}_2\text{O} + 4\text{e}^- \rightarrow 4\text{OH}^-$ ) pathway, where the stability of the  $\text{OM}^*$  and  $\text{OOHM}^*$  intermediates obtained after the adsorption of  $\text{O}_2$  on the surface of the electrocatalysts defines which pathway will be dominant [31,33,35]. The overall

reaction ( $O_2 + 2H_2O + 4e^- \rightarrow 4OH^-$ ) is presented in detail by the following equations (Equations (9)–(12)):



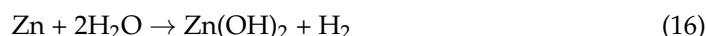
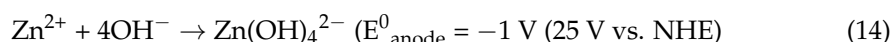
In the first reaction (Equation (9)), an  $O_2$  molecule is adsorbed on the active site of the surface of the electrocatalysts, forming the  $OOHM^*$  intermediate, which subsequently transforms into  $OM^*$  (Equation (10)) intermediates by breaking the O-O bond, finally producing an  $OHM^*$  intermediate (Equation (11)) [38]. This ORR pathway is called associative by W. Xia et al. [38], while the two-electron or peroxy (or second associative) pathway starts by forming  $OOHM^*$  and  $HOOHM^*$  intermediates immediately after the adsorption of the  $O_2$  molecule and without breaking the O-O bond [38]. The third or dissociation ORR pathway is the simplest, where the O-O bond is broken, followed by the formation of an  $OM^*$  intermediate that is reduced to  $OHM^*$  and  $H_2OM^*$  [38]. Depending on the conditions and different electrocatalysts, the ORR could occur via three pathways defined by free-energy barriers [38]. Kinetically, the ORR reaction is intensely sluggish because of the transfer of four coupled electrons and protons and the strong O-O bond, which is difficult to break [39].

#### 4. ORR Catalysts

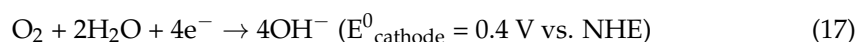
##### 4.1. The ORR Catalysts for Zn–Air Batteries

Zn–air batteries (ZABs) consist of zinc metal and air electrodes as the anode and cathode, respectively. An air electrode comprises a separator, catalyst, and gas diffusion layer. The oxygen inside ZABs is in its gaseous state, because its solubility at atmospheric pressure in the liquid state is low [40]. The anode and cathode electrochemical reactions in an alkaline solution in ZABs are given by the following equations (Equations (13)–(17)) [40]:

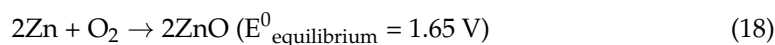
Anode:



Cathode:



Overall reaction:



The equilibrium potential ( $E_{\text{equilibrium}}^0$ ) of ZABs has been calculated as 1.65 V [40]. It is common knowledge that noble platinum (Pt) and/or platinum-based electrocatalysts show the best activity for the ORR [25,41,42]. Still, their scarcity, high price, and poor durability limit their practical application. Nowadays, much research is focused on designing electrocatalysts with a low cost, high ORR activity, and good stability. Different sizes of metallic atoms in metal complex electrocatalysts and their electronegativity could lead

to the redistribution of central electrons, thus optimising electrocatalysts' activity for the ORR [43].

Additionally, the low spin could be changed to the intermediate spin of the metal single-atom site by adding metallic nanoclusters. This could further activate the O-O bond and improve the kinetics of the ORR [43]. The high ORR activity of some metal nanoparticle complexes depends on particle size, i.e., it increases with a decreasing particle size [44]. The appropriate metal–metal bond distance, the increased vacancy of the d electron, and the surface roughness of electrocatalysts can also enhance the ORR activity [44]. The activation of  $O_2$  molecules and the desorption of  $OH^*$  species on active sites due to the presence of metal nanoparticles and single-atomic sites could improve the ORR rate [44].

M. Zhang et al. [25] presented some of these ORR electrocatalysts [25]. Namely, they synthesised electrocatalysts comprising ruthenium cobalt (RuCo) nanoparticles and Co nitrogen ( $N_x$ ) species in N-doped carbon (RuCo@Co-N-C) and examined them for the ORR. The investigation of RuCo@Co-N-C for potential application in ZABs as an air cathode showed better battery performance than Pt/C with ruthenium oxide (Pt/C + RuO<sub>2</sub>). The ZAB's open-circuit voltage ( $E_{OCV}$ ) was found to be 1.45 and 1.39 V for RuCo@Co-N-C and Pt/C + RuO<sub>2</sub>, respectively [25]. A peak power density ( $P_{max}$ ) of 154.3 mW cm<sup>-2</sup> and a specific capacity of 767.4 mAh g<sup>-1</sup> Zn were obtained with RuCo@Co-N-C, higher than with the Pt/C + RuO<sub>2</sub> electrode (Table 2). The 100 h charge/discharge cycling ZAB test of RuCo@Co-N-C and the Pt/C + RuO<sub>2</sub> counterpart showed that the voltage change was not significantly pronounced in the case of RuCo@Co-N-C, as in the case of the Pt/C + RuO<sub>2</sub> counterpart in the ZAB. The outstanding ORR activity of RuCo@Co-N-C was explained by density functional theory (DFT) calculations, indicating that Ru@CoN<sub>4</sub> has a higher charge density than Co@CoN<sub>4</sub>. Also, DFT results showed that Ru/Co and CoN<sub>x</sub> species could act as active sites for improving ORR kinetics.

Fe nanoparticles (Fe NPs) incorporated into nitrogen-doped carbon to provide single Fe atoms (Fe SAs/NPs@NC) showed excellent ORR performance in a ZAB [26]. The ZAB construction consisted of a Zn plate as an anode, an Fe SAs/NPs@NC + IrO<sub>2</sub> air electrode employed as the cathode, and 6 M KOH + 0.2 M Zn(Ac)<sub>2</sub> as the electrolyte. The battery performance of the Fe SAs/NPs@NC + IrO<sub>2</sub> electrode was compared to that of a Pt/C + IrO<sub>2</sub> electrode. The  $E_{OCV}$  of the ZAB was found to be 1.446 and 1.477 V for the Fe SAs/NPs@NC + IrO<sub>2</sub> and Pt/C + IrO<sub>2</sub> electrodes, respectively.  $P_{max}$  values of 107.9 and 92.9 mW cm<sup>-2</sup> and specific capacity values of 734.5 and 658.3 mAh g<sup>-1</sup> at a discharge current density of 10 mA cm<sup>-2</sup> were obtained for the Fe SAs/NPs@NC + IrO<sub>2</sub> and Pt/C + IrO<sub>2</sub> electrodes, respectively. The Fe SAs/NPs@NC + IrO<sub>2</sub> air electrode performed better in the ORR than the Pt/C + IrO<sub>2</sub> electrode. The durability of the ZAB was tested over 1000 cycles for 183 h, and the ZAB with the Fe SAs/NPs@NC + IrO<sub>2</sub> catalyst exhibited excellent durability for all 183 h, while the ZAB with the Pt/C + IrO<sub>2</sub> catalyst could be cycled for only 90 h, exhibiting low durability [26]. It was noticed that atomically dispersed Fe-N<sub>x</sub> and Fe NPs had a strong interaction in the Fe-N<sub>x</sub> structure, which could have led to this remarkable ORR behavior. This strong interaction could have decreased the binding energies of the ORR intermediates and lead to high ORR performances [26].

The oxidation polymerisation–pyrolysis method was used to prepare the uniformly F-doped porous Fe-N/C catalysts by utilising 4-fluoroaniline as a “self-co-doping” precursor with N and F elements (F-FeNC) [27]. Zn foil, F-FeNC, and 6.0 M KOH + 0.2 M Zn(Ac)<sub>2</sub> solution served as an anode, air cathode, and electrolyte in the liquid-state ZAB, respectively. The ORR performance of the FeNC-based ZAB air cathode was compared with that of a Pt/C + IrO<sub>2</sub> cathode in the same conditions. The  $E_{OCV}$  of 1.49 V for the FeNC-based ZAB was superior to the value of 1.44 V for the Pt/C + IrO<sub>2</sub>-based ZAB. The  $P_{max}$  values of 141 and 222 mW cm<sup>-2</sup> at discharge current densities of 222 and 187 mA cm<sup>-2</sup> were found for the FeNC-based ZAB and Pt/C + IrO<sub>2</sub>-based ZAB electrodes, respectively. The high ORR performance of the FeNC-based ZAB was confirmed by comparing the discharging voltages at current densities from 2 to 100 mA cm<sup>-2</sup>, and the FeNC-based ZAB showed a stable discharge platform. The F-FeNC-based ZAB gave a stable discharge voltage of

around 1.28 V at a discharge current density of 10 mA cm<sup>-2</sup> over 80 h. Additionally, the ZAB with the F-FeNC cathode showed a higher specific capacity of 760 mAh g<sup>-1</sup> Zn than the Pt/C + IrO<sub>2</sub>-based ZAB with a value of 721 mAh g<sup>-1</sup> Zn at 10 mA cm<sup>-2</sup> [27]. The F-FeNC-based ZAB air cathode showed long-term cycle stability and good rechargeability for 120 h, while the Pt/C + IrO<sub>2</sub>-based ZAB showed cycle stability for about 50 h. It was explained that the electronic structure of Fe-N<sub>x</sub> active sites could be optimised by incorporating F, while 4-FA mitigated Fe aggregation. The excellent ORR performance of the F-FeNC catalyst was due to its specific structure with homogeneously dispersed F atoms and abundant Fe-N<sub>x</sub> active sites [27].

**Table 2.** Performance of the newest ORR electrocatalysts and the corresponding ZABs.

ORR Air Cathode	E <sub>OCV</sub> (V) vs. RHE	E <sub>1/2</sub> (V) vs. RHE	Durability	P <sub>max</sub> (mW cm <sup>-2</sup> )	Specific Capacity (mAh g <sup>-1</sup> )	Ref.
RuCo@Co-N-C	1.45	0.90	Long-term cyclic stability for 100 h.	154.3 at ~0.69 V and ~225 mA cm <sup>-2</sup>	767.4	[25]
Pt/C + RuO <sub>2</sub>	1.39	/	/	119.8 at ~0.57 V and ~210 mA cm <sup>-2</sup>	717.0	[25]
Fe SAs/NPs@NC + IrO <sub>2</sub>	1.446	/	Excellent durability of 1000 cycles over 183 h.	107.9 at ~0.83 V and ~130 mA cm <sup>-2</sup>	734.5 at 10 mA cm <sup>-2</sup>	[26]
Pt/C + IrO <sub>2</sub>	1.477	/	Low durability for 90 h.	92.9 at ~0.80 V and ~115 mA cm <sup>-2</sup>	658.3 at 10 mA cm <sup>-2</sup>	[26]
Fe-FeNC	1.49	0.82	Long-term cyclic durability for 120 h.	141 at ~0.63 V and 222 mA cm <sup>-2</sup>	760 at 10 mA cm <sup>-2</sup>	[27]
0.05 Mn-N-P-C	1.45	0.82	The ZAB mechanically recharged multiple times within 80 h without the degradation of voltage.	133 at ~0.71 V and ~188 mA cm <sup>-2</sup>	830 at 5 mA cm <sup>-2</sup>	[28]
Te/Fe-N-C	1.49	0.88	ΔE = 22 mV (50,000 s).	250 at ~0.71 V and ~350 mA cm <sup>-2</sup>	770 at 20 mA cm <sup>-2</sup>	[29]
FeNC-Ce-950	1.480	0.921	The ZAB's charge/discharge voltages with FeNC-Ce-950 were high for about 11 h.	175 at ~0.69 V and 255 mA cm <sup>-2</sup>	757 at 10 mA cm <sup>-2</sup>	[43]
Co SAs/NCNA	1.49	0.98	/	206 at ~0.59 V and ~350 mA cm <sup>-2</sup>	769	[44]
FeNFC800	1.56	0.829	Galvanostatic discharge curve at 10 mA cm <sup>-2</sup> for 20,000 s.	196 at ~0.78 V and ~250 mA cm <sup>-2</sup>	/	[45]
0.4Co@NC-900	1.50	0.91	Excellent stability after long-term charge-discharge cycling tests over 130 h.	203 at ~0.62 V and 325 mA cm <sup>-2</sup>	792	[46]
N-G/CNTs-900	1.45	0.838	Two N-G/CNTs-900-based ZABs were connected in series with an electronic light display screen for more than 24 h.	133.6 at ~0.61 V and 220.10 mA cm <sup>-2</sup>	707 at 10 mA cm <sup>-2</sup>	[47]
P-Fe-N-CNTs	1.498	0.8843	The durability of the ZAB was satisfactory, and the voltage retention rate was 95.1% after 144 h.	145 at ~0.64 V and ~225 mA cm <sup>-2</sup>	885 at 10 mA cm <sup>-2</sup>	[48]
Co@N-HPCFs	/	0.831	The excellent electrochemical stability of the Co@N-HPCF-800-based ZAB was observed in a long-term test with 600 cycles (200 h) at 2 mA cm <sup>-2</sup> .	136.2 at ~0.53 V and ~255 mA cm <sup>-2</sup>	723 at 5 mA cm <sup>-2</sup>	[49]
NPS-HPCNs	1.479	0.86	The 200 h long-term cycling test of the NPS-HPCN-based battery at a current density of 10 mA cm <sup>-2</sup> showed reinforced charge and discharge potentials.	206 at ~0.59 V and ~350 mA cm <sup>-2</sup>	/	[50]

Mn-N-P-doped carbon spheres were synthesised by the polymerisation of hexachlorotriphosphazene (HCCP) and phloroglucinol, followed by calcination at 900 °C [28]. J. Li et al. presented a ZAB with a 0.05 Mn-N-P-C air cathode and a Zn sheet as an anode in 6 M KOH, which delivered an E<sub>OCV</sub> of 1.45 V and a P<sub>max</sub> of 133 mW cm<sup>-2</sup>. The Mn-N-P-C air cathode showed better ORR performance than commercial Pt/C catalysts. This ZAB was mechanically recharged numerous times over 80 h with no voltage degradation. Theoretical calculations showed that introducing Mn into N-P-doped carbon decreased the dissociation barrier from O<sub>2</sub> to O<sup>\*</sup>, which led to the high ORR catalytic activity of the Mn-N-P-C catalyst [28].

Pyrolysis-acquired iron and nitrogen-co-doped carbon (Fe-N-C) was prepared. After that, the Fe-N-C was mixed with tellurium (Te) by micelle-induced polymerisation with Te nanowires as an in situ intervening agent (Te/Fe-N-C) [29]. A homemade ZAB with a

Te/Fe-N-C air cathode showed an  $E_{ocv}$  and  $P_{max}$  of 1.49 V and 250 mW cm<sup>-2</sup>, respectively. These values illustrated the better ORR performance of the Te/Fe-N-C compared to the Pt/C air cathode in the ZAB. Additionally, the discharge stability of Te/Fe-N-C and Pt/C was examined at 5 and 20 mA cm<sup>-2</sup>, and discharge voltages of 1.30 and 1.22 V were obtained for Te/Fe-N-C and values of 1.28 and 1.19 V for Pt/C, respectively. Long-term discharge durability tests with Te/Fe-N-C and Pt/C were carried out on the ZAB at 5 and 20 mA cm<sup>-2</sup> for 50,000 s. This test of the ZAB showed a low voltage change ( $\Delta E$ ) of 22 mV for the Te/Fe-N-C electrode. The discharge-specific capacity of Te/Fe-N-C was calculated to be 770 mAh g<sup>-1</sup><sub>Zn</sub> at 20 mA cm<sup>-2</sup>. Finally, the discharge voltages (1.325, 1.300, 1.275, 1.240, and 1.327 V) for Te/Fe-N-C at all current densities (2, 5, 10, 20, and 5 mA cm<sup>-2</sup>) were higher than for Pt/C. The content of Fe on the surface of the Te/Fe-N-C catalyst was 0.38%, and the Fe with both +2 and +3 valences was bonded with N. Then, Te would bond with the Fe-N<sub>x</sub> out of the plane, resulting in the improvement of the N content on the material surface and increasing the ORR activity of the Te/Fe-N-C catalyst [29].

Cerium oxides (CeO<sub>x</sub>) were added into the two-dimensional co-doped carbon (Fe-N-C) catalyst (FeNC-Ce-950) [43]. ZAB tests were carried out with FeNC-Ce-950 as an air cathode catalyst, a zinc plate as an anode, and 6 M KOH as an electrolyte. The  $E_{ocv}$  of the ZAB with FeNC-Ce-950 was observed to be 1.480 V (Figure 1b). Figure 1c shows the 2 V light-emitting diode connected to two Zn-air batteries with FeNC-Ce-950 in series.  $P_{max}$  and specific capacity values of 175 mW cm<sup>-2</sup> and 757 mAh g<sup>-1</sup><sub>Zn</sub>, respectively, were obtained for the FeNC-Ce-950-assembled battery (Figure 1d,e), and the specific capacity was determined by normalising the consumed Zn ( $m = 1.9$  g) at a discharge current density of 10 mA cm<sup>-2</sup>. The ZAB's charge/discharge voltages with FeNC-Ce-950 were high for about 11 h (Figure 1f) [43]. The FeNC-Ce-950 catalyst consisted of a vital Ce<sup>4+</sup>/Ce<sup>3+</sup> redox system with a high number of oxygen vacancies correlated to highly efficient O<sub>2</sub> adsorption and a higher number of carbon matrix defects than the Ce-free Fe-N-C catalysts [43].

Co-N<sub>4</sub> sites on N-doped carbon nanofibre aerogel (Co SAs/NCNA) were constructed by the direct and green pyrolysis of a metal-chelated cellulose nanofibre (TOCNFs-Cd<sup>2+</sup>/Co<sup>2+</sup>) hydrogel precursor [44]. An  $E_{ocv}$  of 1.49 V was obtained for the ZAB with a Co SAs/NCNA air cathode. Also, the performance of this battery with Co SAs/NCNA in terms of specific capacity and  $P_{max}$  was found to be 769 mAh g<sup>-1</sup> and 206 mW cm<sup>-2</sup>, respectively. The Co SAs/NCNA consisting of 3D hierarchically porous carbon aerogels showed excellent ORR kinetics in alkaline media [44].

A. Yu et al. [45] synthesised Fe/N/F-tri-doped (FeNFCs) carbon nanotubes (CNTs) by annealing the post-synthesised trifluoroacetic anhydride-modified Fe-MIL-88B-NH<sub>2</sub> nanocrystals with melamine in an N<sub>2</sub> atmosphere at high temperature (Scheme 3). The authors prepared a homemade ZAB with an FeNFC800 catalyst (loading mass = 1 mg cm<sup>-2</sup>), Zn plate, and 6 M KOH solution as the air cathode, the anode, and the electrolyte, respectively. This battery with the FeNFC800 catalyst gave an  $E_{ocv}$  of 1.56 V, showing a higher cell voltage than the value of 1.47 V obtained for the ZAB with a 20% Pt/C air cathode. Potential practical applications of the FeNFC800 air cathode were examined by the galvanostatic discharge curve at 10 mA cm<sup>-2</sup> for 20,000 s. A  $P_{max}$  of 196 mW cm<sup>-2</sup> was obtained for the FeNFC800 air cathode, which was higher than the value of 56 mW cm<sup>-2</sup> for commercial Pt/C. It was confirmed that FeNFC800 has a unique structure with a dominant CNT content, which provides a high pyridinic/graphitic nitrogen content, a large specific surface area, ionic/semi-ionic C-F bonds, etc. These structural facts could have led to the high ORR activity of the FeNFC800 catalyst [45].

A novel nanocapsule with a cobalt core and nitrogen-doped carbon shells (Co@NC) supported on a metal-organic framework (MOF)-derived hierarchical porous carbon framework (0.4Co@NC-900) was examined as an air cathode in a liquid ZAB [46]. Specifically, the primary ZAB was constructed with a Zn plate anode, 0.4Co@NC-900 air electrode, and 6 M KOH + 0.2 M zinc acetate solution. This ZAB gave an  $E_{ocv}$  of 1.50 V and a  $P_{max}$  of 203 mW cm<sup>-2</sup>. These excellent battery performance metrics could have resulted from the unique pore structures of the 0.4Co@NC-900 electrocatalyst. The battery performance of

the 0.4Co@NC-900-based and Pt/C-based batteries was investigated at different current densities (2, 5, 10, 20, 10, and 5  $\text{mA cm}^{-2}$ ). The 0.4Co@NC-900-based battery showed a higher discharge voltage at all current densities than the Pt/C-based ZAB. Precisely, the discharge voltage of the 0.4Co@NC-900-based battery decreased by only 5.7% with the current density increasing from 2 to 20  $\text{mA cm}^{-2}$ . Specific capacity values of 792 and 611  $\text{mAh g}^{-1}$  were obtained for the 0.4Co@NC-900-based and Pt/C-based ZABs, respectively. Most importantly, the 0.4Co@NC-900-based battery showed excellent stability after long-term charge–discharge cycling tests over 130 h with deviations in the charge–discharge voltage of 0.2 V. The excellent ORR activity and stability of the 0.4Co@NC-900 catalyst were obtained due to its mesoporous structure, with the optimised micro-/mesoporous ratio of carbon structures decreasing the chemical corrosion of the Co nanoparticles [46].

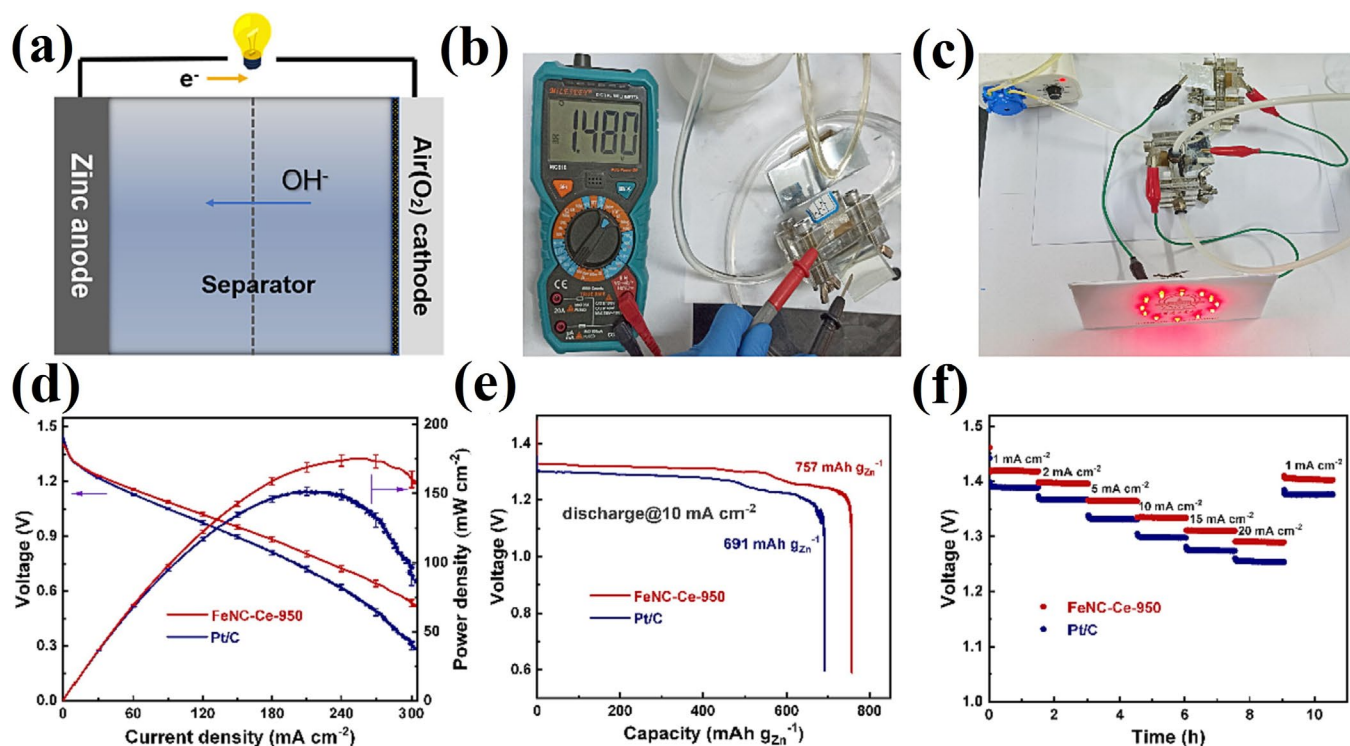
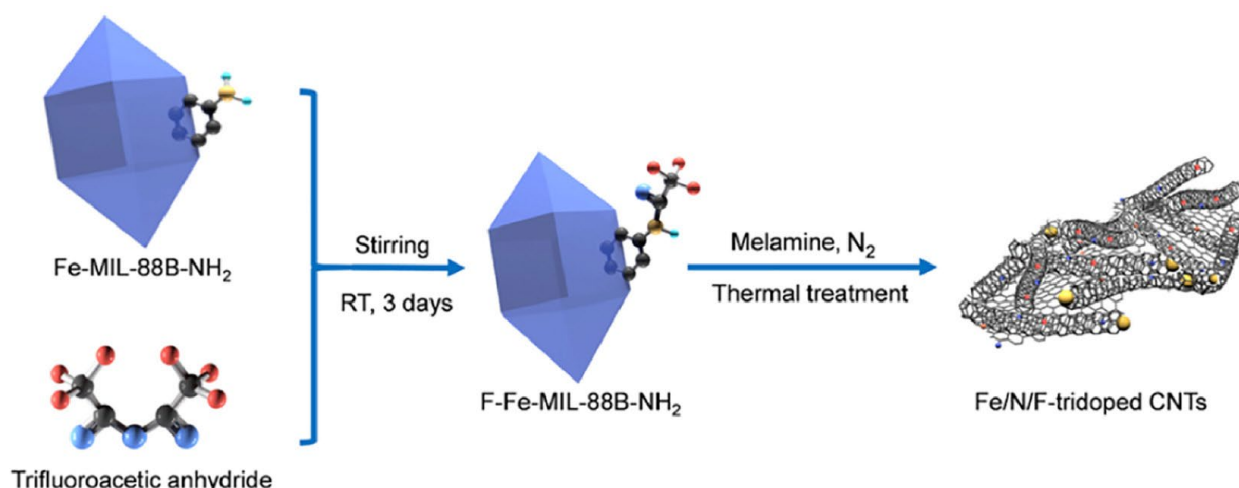


**Figure 1.** Scheme of Zn–air batteries (a),  $E_{\text{OCV}}$  of an FeNC-Ce-950-assembled ZAB measured by a multimeter (b), light-emitting diode lit with two FeNC-Ce-950-assembled ZABs in series (c), polarisation and power density plots of ZAB with FeNC-Ce-950 and Pt/C (d), long-term discharge test for ZABs with FeNC-Ce-950 and Pt/C (e), constant current charge/discharge test controlling current densities for ZABs assembled from FeNC-Ce-950 and Pt/C (f) [43]. Copyright 2023, *Journal of Colloid and Interface Science*.

A hybrid heterostructure N-G/CNTs-900 catalyst with a hierarchically porous architecture was prepared by the hydrothermal reduction self-assembly method using graphene oxide (GO), carbon nanotubes (CNTs), and CNTs combined with urea as the precursor, nitrogen source, and foam-introducing agent, respectively [47]. A liquid rechargeable ZAB was constructed of zinc with a thickness of 0.5 mm as an anode, N-G/CNTs-900 as an air cathode, and 6.0 M KOH + 0.2 M zinc acetate as an electrolyte. The ZAB with the N-G/CNTs-900 air electrode gave an  $E_{\text{OCV}}$  of 1.45 V and a  $P_{\text{max}}$  of 133.6  $\text{mW cm}^{-2}$ . This battery showed a specific capacity of 707  $\text{mAh g}^{-1}$  at 10  $\text{mA cm}^{-2}$ . The authors presented the high activity and stability of N-G/CNTs-900 as an air cathode by connecting two N-G/CNTs-900-based ZABs in series with an electronic light display screen for more than 24 h [47].



**Scheme 3.** Procedure for the preparation of FeNFC800 catalysts [45]. Copyright 2023, *Chinese Chemical Letters*.

An Fe/N/P-tri-doped prolonged carbon nanotube (P-Fe-N-CNT) electrocatalyst with a large specific surface area and abundant porous structure was prepared according to a facile one-step calcination procedure and tested for the ORR in a ZAB [48]. Ni foam containing a P-Fe-N-CNT catalyst with a catalyst load of  $1 \text{ mg cm}^{-2}$  and a polished Zn sheet were set as the cathode and anode in the ZAB (Figure 2a), respectively, while  $6 \text{ M KOH} + 0.2 \text{ M Zn (Ac)}_2$  was used as the electrolyte. The assembled ZAB with the P-Fe-N-CNT air cathode gave an  $E_{\text{OCV}}$  of  $1.498 \text{ V}$  (Figure 2b). A  $P_{\text{max}}$  of  $145 \text{ mW cm}^{-2}$  and a discharge specific capacity of  $885 \text{ mAh g}^{-1}$  at  $10 \text{ mA cm}^{-2}$  was obtained for this P-Fe-N-CNT-based ZAB (Figure 2c,f). The P-Fe-N-CNT catalyst provided an excellent rate performance for the ZAB (Figure 2d) at different current densities ( $1, 2, 5, 10, 15, 20, 25$ , and  $10 \text{ mA cm}^{-2}$ ). The assembled ZAB with the P-Fe-N-CNT air cathode provided satisfactory durability and a voltage retention rate of  $95.1\%$  after  $144 \text{ h}$  at  $10 \text{ mA cm}^{-2}$  (Figure 2e). In all cases, the battery performance of the P-Fe-N-CNT air cathode was found to be better than that of a Pt/C air cathode. The authors performed an electrochemical impedance spectroscopy (EIS) investigation of the P-Fe-N-CNT- and Pt/C-based ZABs. The P-Fe-N-CNT-based ZAB gave a lower charge transfer resistance than the Pt/C catalyst, showing improved conductivity. This remarkable ORR activity of the P-Fe-N-CNT catalyst was due to the synergistic effect of Fe-Nx/Px and N- and P-co-doped carbon, which provided a unique structure with a large specific surface area, promoting a high rate of charge and mass transfer [48].

The highly dispersed Co nanoparticles on a hierarchically porous N-doped carbon fibre (Co@N-HPCF) catalyst were also explored for use in MABs [49]. The liquid ZAB was assembled using a zinc plate as the anode, a Co@N-HPCF-800 catalyst as the air cathode (catalyst loading of  $1 \text{ mg cm}^{-2}$ ), and  $6 \text{ M KOH} + 0.2 \text{ M zinc acetate}$  solution as the electrolyte. The Co@N-HPCF-800-based ZAB showed a higher discharge voltage than the 20 wt% Pt/C-based battery at the same current density and a substantially higher voltage at a high current density. Specifically, the Co@N-HPCF-800-based battery gave a  $P_{\text{max}}$  of  $136.2 \text{ mW cm}^{-2}$  and a specific capacity of  $723 \text{ mAh g}^{-1}$  at  $5 \text{ mA cm}^{-2}$ . Interestingly, the Co@N-HPCF-800-based battery gave a 1.43-times higher  $P_{\text{max}}$  than the 20 wt% Pt/C-based battery. The relatively stable charge-discharge platform of the ZAB with the Co@N-HPCF-800 cathode was demonstrated during a long-term test over 600 cycles (200 h) at  $2 \text{ mA cm}^{-2}$ . The charge-discharge efficiency decreased from the initial 64.5 to 57.1%, which presented the excellent electrochemical stability of the Co@N-HPCF-800-based ZAB. The outstanding electrocatalytic ORR performance of the Co@N-HPCF electrocatalyst was explained by its unique structure and appropriate synergistic effects. Improved mass transport for ORR species was noticed by the rapid diffusion of a substance through its hollow porous nanostructured structures. The enhanced electron structure was achieved by its 1D structure [49].

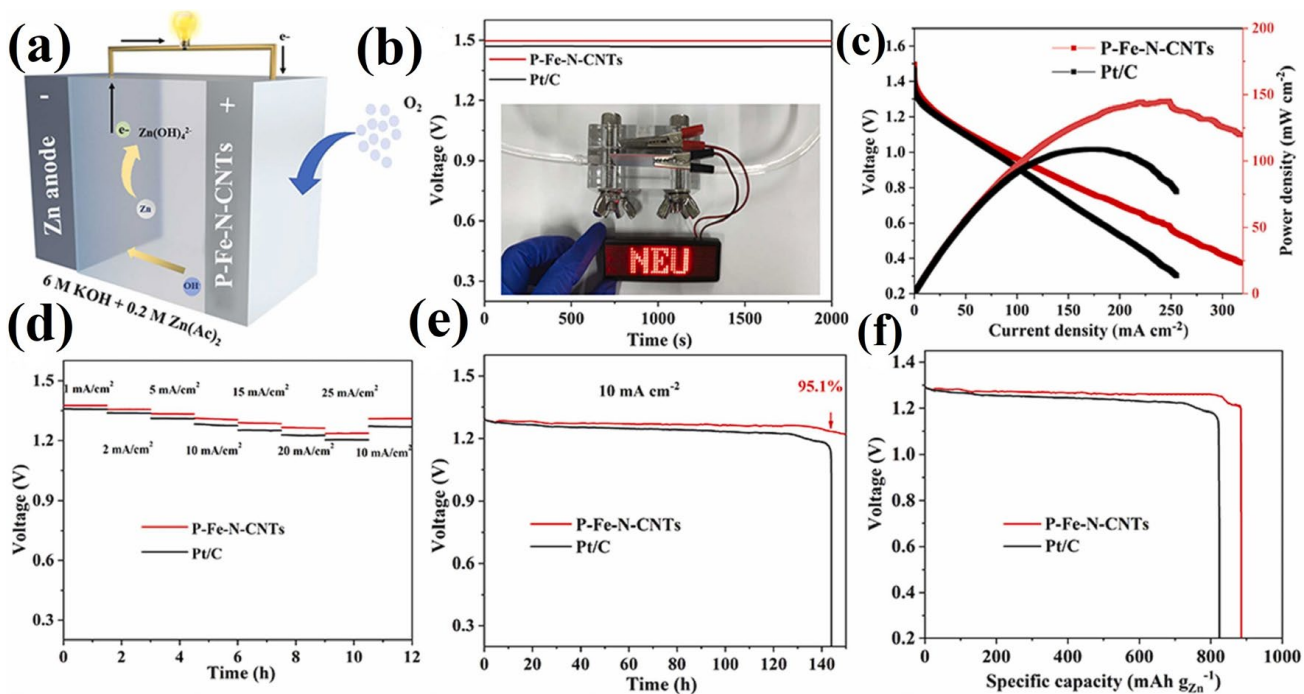


**Figure 2.** Scheme of the ZAB (a), OCV curves and the ZAB configuration in inset (b), discharge polarisation curves (c), rate performance (d), cycle performance (e), specific capacity curves at  $10 \text{ mA cm}^{-2}$  for P-Fe-N-CNT- and Pt/C-based ZABs (f) [48]. Copyright 2023, *Applied Catalysis B: Environmental*.

Q. Zhao et al. [50] presented a metal-free and novel coating strategy to produce adjacent N, P, and S-co-doped hierarchical porous carbon nanoshells (NPS-HPCNs) that were highly active for the ORR. Additionally, NPS-HPCNs served as the air cathode, a polished zinc plate as the anode, and 6 M KOH containing 0.2 M  $\text{Zn}(\text{OAc})_2$  solution as the electrolyte in a primary ZAB. An  $E_{\text{OCV}}$  of 1.479 V and a  $P_{\text{max}}$  of  $206 \text{ mW cm}^{-2}$  were obtained for the NPS-HPCN-based ZAB. It was noticed that the galvanostatic discharge voltages of the NPS-HPCN-based battery decreased with an increased current density from 1 to  $15 \text{ mA cm}^{-2}$ . The galvanostatic discharge voltage plateaus of the NPS-HPCN-based battery appeared at 1.37, 1.34, 1.33, 1.32, 1.31, and 1.29 V, corresponding to the discharge current densities of 1, 3, 5, 7, 10, and  $15 \text{ mA cm}^{-2}$ , respectively. A 200 h long-term cycling test of the NPS-HPCN-based battery at a current density of  $10 \text{ mA cm}^{-2}$  showed reinforced charge and discharge potentials. The porous hollow structure of the NPS-HPCN electrocatalyst could improve the mass and electron transfer during the ORR. N, P, and S atoms could reduce the energy barriers for the ORR and enhance the adsorption of  $\text{O}_2$  [50].

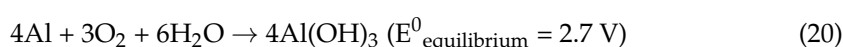
#### 4.2. ORR Catalysts for Aluminium-air Batteries

Aluminium-air batteries (AABs) have also been explored as future energy generation storage devices. AABs have a high theoretical voltage (2.7 V), high energy density ( $8.1 \text{ kWh kg}^{-1}$ ), high theoretical specific capacity of  $2.98 \text{ Ah g}^{-1}$ , low cost, abundant reserves, and light weight [51,52]. These batteries are assembled with an aluminium anode, an air cathode, and an alkaline or neutral electrolyte such as KOH, NaO, or NaCl [51]. The anode (Equation (19)) and cathode electrochemical reactions (Equation (17)) in an alkaline solution in AABs are given by the following equations (Equations (17) and (19)) [40]:

Anode:



Overall reaction:



Herein, we focus on the newest air cathode materials, essential components in AABs. We report several of the newest catalytic active layers consisting of an electrocatalyst, carbon material, and binder, which correspond to the ORR.

Cobalt nanoparticles encapsulated with N-doped graphene nanoplatelets (Co@N/GNPs) were prepared by plasma engineering [53]. This electrocatalyst was set as an air cathode with a diameter of 0.5 mm and catalyst loading of  $2 \text{ mg cm}^{-2}$ , an Al 5052 alloy plate was set as an anode; and a 6 M KOH solution was set as the electrolyte with dissolved 0.01 M  $\text{Na}_2\text{SnO}_3$ , 0.0005 M  $\text{In(OH)}_3$ , and 0.0075 M ZnO as the corrosion inhibitor in homemade AABs. The  $E_{\text{ocv}}$  and  $P_{\text{max}}$  of the AABs with a Co@N/GNP cathode were founded to be 1.40 V and  $143.4 \text{ mW cm}^{-2}$  (Table 3), respectively. The discharge plots at different current densities (5, 25, 50, 100, and  $5 \text{ mA cm}^{-2}$ ) for 10 min showed that the discharge potential of the Co@N/GNPs reached 1.04 V at a current density of  $100 \text{ mA cm}^{-2}$ . The durability of this Al-air battery was investigated at  $25 \text{ mA cm}^{-2}$ , where it was noticed that the Co@N/GNP cathode presented voltage degradation at 29,460 s. The authors compared the battery performances of AABs with a Co@N/GNP cathode and a graphene nanoplate (GNP) cathode, and the results showed better battery performance for the Co@N/GNP cathode due to the incorporation of the cobalt by the n-doped carbon shell [53].

**Table 3.** The performance of the newest ORR electrocatalysts and the corresponding AABs.

ORR Air Cathode	$E_{\text{ocv}}$ (V) vs. RHE	$E_{1/2}$ (V) vs. RHE	Durability	$P_{\text{max}}$ ( $\text{mW cm}^{-2}$ )	Specific Capacity ( $\text{mAh g}^{-1}$ )	Ref.
Co@N/GNP	1.40	0.98	The durability of this AAB was investigated at $25 \text{ mA cm}^{-2}$ , and it was noticed that the Co@N/GNP cathode showed voltage degradation at 29,460 s.	143.04 at $0.74 \text{ V}$ and $191.83 \text{ mA cm}^{-2}$	/	[53]
Integrated B-N-G	/	0.868	High durability of AAB construction.	152.4 at $\sim 0.81 \text{ V}$ and $\sim 188 \text{ mA cm}^{-2}$	/	[52]
Slurry-cast B-N-G	/	/	/	137.1 at $\sim 0.78 \text{ V}$ and $\sim 175 \text{ mA cm}^{-2}$	/	[52]
Pt/C	/	0.854	/	136.2 at $\sim 0.64 \text{ V}$ and $\sim 212 \text{ mA cm}^{-2}$	/	[52]
FePc@Co-SAs/PCNF		0.87	/	196.36 at $\sim 0.79 \text{ V}$ and $\sim 250 \text{ mA cm}^{-2}$	/	[54]
Co-N-C	1.7	0.838	After 20000 s, retained 95% of the performance.	148 at $\sim 0.99 \text{ V}$ and $\sim 150 \text{ mA cm}^{-2}$	1148 at $50 \text{ mA cm}^{-2}$	[55]

Boronate-amino (B–N) coordinated active sites deposited on a graphene aerogel (denoted as B–N–G) were investigated for the ORR in alkaline media [52]. Then, an Al-air homemade battery was constructed with B–N–G on a Ni foam current collector as an integrated air cathode with a thickness of  $\sim 0.5 \text{ mm}$  and an Al 1.0 wt%–Mg 0.1 wt%–Sn (Al–Mg–Sn) alloy as an anode. In the Al-air homemade battery, 4 M NaOH or 3.5% NaCl solution was used as an electrolyte. Explicitly, the performance of the Al-air homemade batteries constructed with an integrated B–N–G air cathode was compared with slurry-cast B–N–G and Pt/C air cathodes. The authors noted that the  $E_{\text{ocv}}$  of the integrated B–N–G-based battery was higher than that of the slurry-cast B–N–G- and Pt/C-based batteries. A  $P_{\text{max}}$  of  $152.4 \text{ mW cm}^{-2}$  was obtained for the integrated B–N–G-based battery, while  $P_{\text{max}}$  values of 137.1 and  $136.2 \text{ mW cm}^{-2}$  were founded for the slurry-cast B–N–G-based (Table 3) and Pt/C-based batteries, respectively. The AAB with the integrated B–N–G air cathode gave larger discharge voltage plateaus at different current densities ranging from 5 to  $100 \text{ mA cm}^{-2}$  than the other two examined batteries. The integrated B–N–G–air cathode-based battery demonstrated that the voltage recovered to 1.71 V when the current density changed to  $5 \text{ mA cm}^{-2}$  again. The long-term discharge curve of the integrated B–N–G–air cathode-based battery was obtained at  $20 \text{ mA cm}^{-2}$  by mechanical charging every 4 h. This battery showed no voltage loss with a constant voltage plateau at  $\sim 1.58 \text{ V}$ . After that, the Al-air battery with the B–N–G–air cathode was tested in contact with a KOH electrolyte and aluminium species after off-loading storage for 5 days in the KOH electrolyte. It was noticed that the discharge voltage remained at 1.55 V, presenting the

good durability of this construction. The intensive ORR activity of the B–N–G catalyst originated from the high activity of the B–N coordinated active sites [52].

Iron phthalocyanine (FePc) anchored on the cobalt-nitrogen sites on N-doped porous carbon nanofibres (FePc@Co-SAs/PCNF) was synthesised and investigated for the ORR [54]. Then, FePc@Co-SAs/PCNF was used as a cathode in a homemade AAB to investigate its practical application in a battery setup. This AAB was assembled with an Al-Mg-Sn alloy plate as the anode and 3.5 wt% NaCl solution as the electrolyte. Stable discharge voltages of 1.58 and 1.28 V were found at 20 and 100 mA cm<sup>-2</sup>. This battery was examined with periodically recharging Al alloy anodes, and no voltage loss during continuous discharge was seen. A  $P_{max}$  of 196.36 mW cm<sup>-2</sup> was obtained for the FePc@Co-SAs/PCNF-based AAB, while the commercial Pt/C-based battery showed a lower value of 131.26 mW cm<sup>-2</sup>. The intensive ORR catalysis by the FePc@Co-SAs/PCNF could have resulted from coupling the FePc with Co-N<sub>3</sub> and their strong electronic interaction, leading to the enhanced adsorption of O<sub>2</sub> [54].

An impregnation method was used for preparing a nitrogen-doped carbon catalyst by heat treatment, and Co anchored on a N-doped carbon catalyst (Co-N-C) with a size of 10–30 nm was prepared [55]. The homemade AAB consisted of an Al–Mg–Sn–In alloy plate as the anode, the Co-N-C catalyst as the air cathode, and 6 M of KOH with 0.5% sodium stannate as the electrolyte. An  $E_{ocv}$  of 1.7 V and a  $P_{max}$  of 148 mW cm<sup>-2</sup> were obtained for the Co-N-C-based AAB. This battery performance was somewhat better than that obtained for a 20wt% Pt/C-based battery. The specific capacity of the AABs was examined at 50 mA cm<sup>-2</sup> and found to be 1148 mAh·g<sup>-1</sup> for the Co-N-C-based AAB and 681 mAh g<sup>-1</sup> for the 20% Pt/C-based AAB. Both air cathodes in the AABs showed good performance at different discharge currents (10, 20, 30, 40, 50, 20, and 10 mA cm<sup>-2</sup>). The durability of the Co-N-C-based AAB was retained at 95% after 20,000 s. The authors [55] presented two Co-N-C-based aluminum-air battery cells in series with a catalyst cathode load of 1 mg cm<sup>-2</sup> and showed that these batteries could charge a mobile phone and light a series of lights simultaneously (Figure 3).

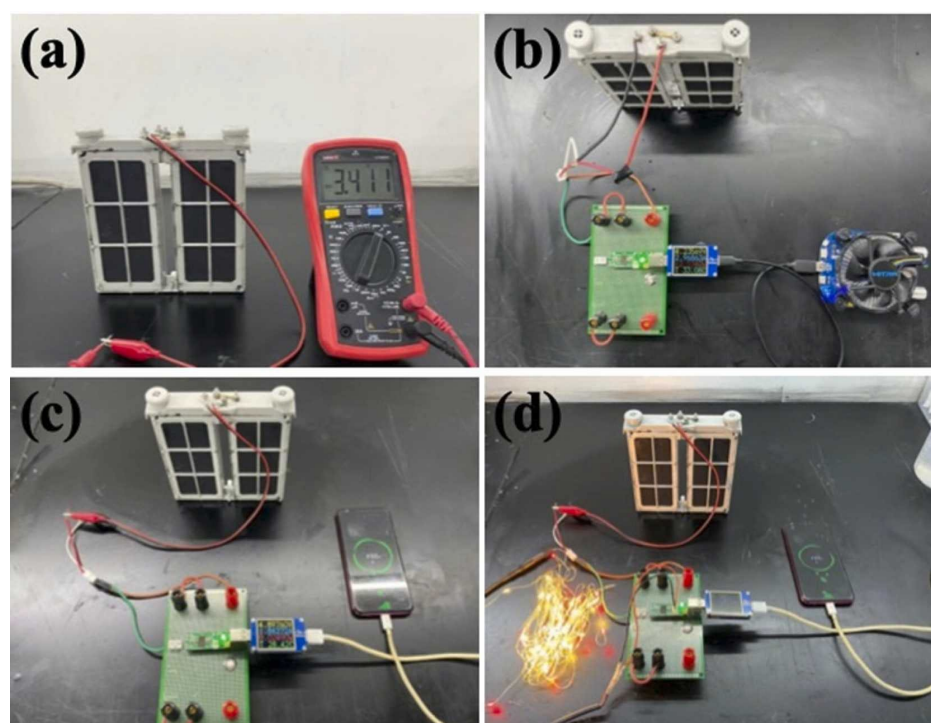


**Figure 3.** Two AABs in series showing an  $E_{ocv}$  of 3.41 V (a), two AABs in series driving a fixed load (b), charging a mobile phone and illuminating the lights (c), charging a mobile phone simultaneously (d) [55]. Copyright 2023, *Applied Catalysis A: General*.

## 5. Bifunctional ORR/OER Catalysts

The development of new bifunctional electrocatalysts for MABs is still challenging due to the slow kinetics of both the OER and ORR in the charge/discharge process. Moreover, the high price and low abundance of noble metals have hindered their use in electrocatalysis. Consequently, low-price and effective bifunctional catalysts are vital to accelerate electrochemical reactions and raise the recharge rate and the voltage of rechargeable MABs.

Recently, transition metal (TM) (Mn, Co, Ni, and Fe)-based materials have shown considerable catalytic activity for the OER/ORR. TM oxides present several crystal structures and active defect sites, benefiting from the existence of different valence states in a TM. Thus, transition metals combined with nitrogen-doped carbons (M/N-C) with excellent ORR/OER performance have been reported as good substitutes for precious metal catalysts [56].

Many studies have been performed on carbon materials (carbon nanotubes, graphite, mesoporous carbon, and graphene, among others), and many strategies for the enhancement of their performance, such as heteroatom-doping, have been introduced. Carbon materials have been extensively explored for the ORR/OER because of their interesting properties, such as their low price, good electronic conductivity, large specific surface area, and high stability. Nevertheless, the electrocatalytic efficiency of pure carbon materials is not expected. Conversely, the synergic effects between carbon materials and other elements can lead to bifunctional behaviour. It has recently been reported that doping carbon materials with, for instance, N, P, S, F, or B, can polarise the carbon atoms due to the size and electronegativity differences between the dopants and carbon. Co-doping carbon materials with heteroatoms of different electronegativities will raise the asymmetry of electrons at the doping position, introducing more active sites for ORR/OER catalysts and promoting the adsorption/desorption of oxygen. An example is the hybrid electrocatalysts composed of transition metal compounds and heteroatom-doped carbon materials cited to increase ORR/OER activity [57,58].

Metal-free N-doped graphdiyne (GDY) was developed as an ORR/OER material [53], and pyridinic N was demonstrated to contribute to enhanced catalytic activity for the ORR and OER. Other studies involving B-, N-, and F-tri-doped lignin-derived carbon nanofibre (BNF-LCF) catalysts showed high catalytic performance for the ORR/OER. Specifically, a lower difference between the potential at 10 mA cm<sup>-2</sup> in OER mode and the E<sub>1/2</sub> in ORR mode of 0.728 V was determined for BNF-LCFs compared to the value of 0.760 V in the case of commercial Pt/C + RuO<sub>2</sub>. The BNF-LCF-based liquid ZABs presented a high OCV of 1.536 V and a high specific capacity of 791.5 mAh g<sup>-1</sup> with considerable charge-discharge cycle efficiency (Figure 4) [59]. One of the most interesting materials is single-atom carbon with M-Nx-C species. Li and coworkers designed an electrocatalyst involving ferric oxide (Fe<sub>3</sub>O<sub>4</sub>) and cobaltous oxide (CoO) in a carbon nanoflower. The Zn-air battery using this electrocatalyst showed an OCV of 1.457 V, a stable discharge of 98 h, a high specific capacity of 740 mAh g<sup>-1</sup>, a large power density of 137 mW cm<sup>-2</sup>, and excellent charge/discharge cycling performance [60]. Electrocatalysts supported on helically coiled nitrogen-doped carbon nanotubes (HNCNTs), such as Co@H-NCNTs, were studied for the ORR and OER and were demonstrated to be comparable with Pt/C and IrO<sub>2</sub> (Figure 5). DFT calculations showed that the active sites in Co@H-NCNTs had low overpotentials for the ORR/OER, leading to remarkable catalytic activity. A Zn-air battery with Co@H-NCNTs exhibited a high power density (207.0 mW cm<sup>-2</sup>) and good stability after 300 cycles. Thus, Co@H-NCNTs could be a favourable bifunctional ORR/OER catalyst for effective electrocatalysis in Zn-air batteries [61].

Transition metal materials (oxides (spinel oxide and perovskite oxide, double-layered hydroxides); sulfides; phosphides; and nitrides) have demonstrated efficiency as precious-metal-free bifunctional electrocatalysts. However, their performance could be influenced by their intrinsic poor conductivity, decelerating the reaction kinetics [62]. Still, recently, nanostructured transition metal phosphides and their hybrids have demonstrated excellent activity and durability for the OER/ORR [56].

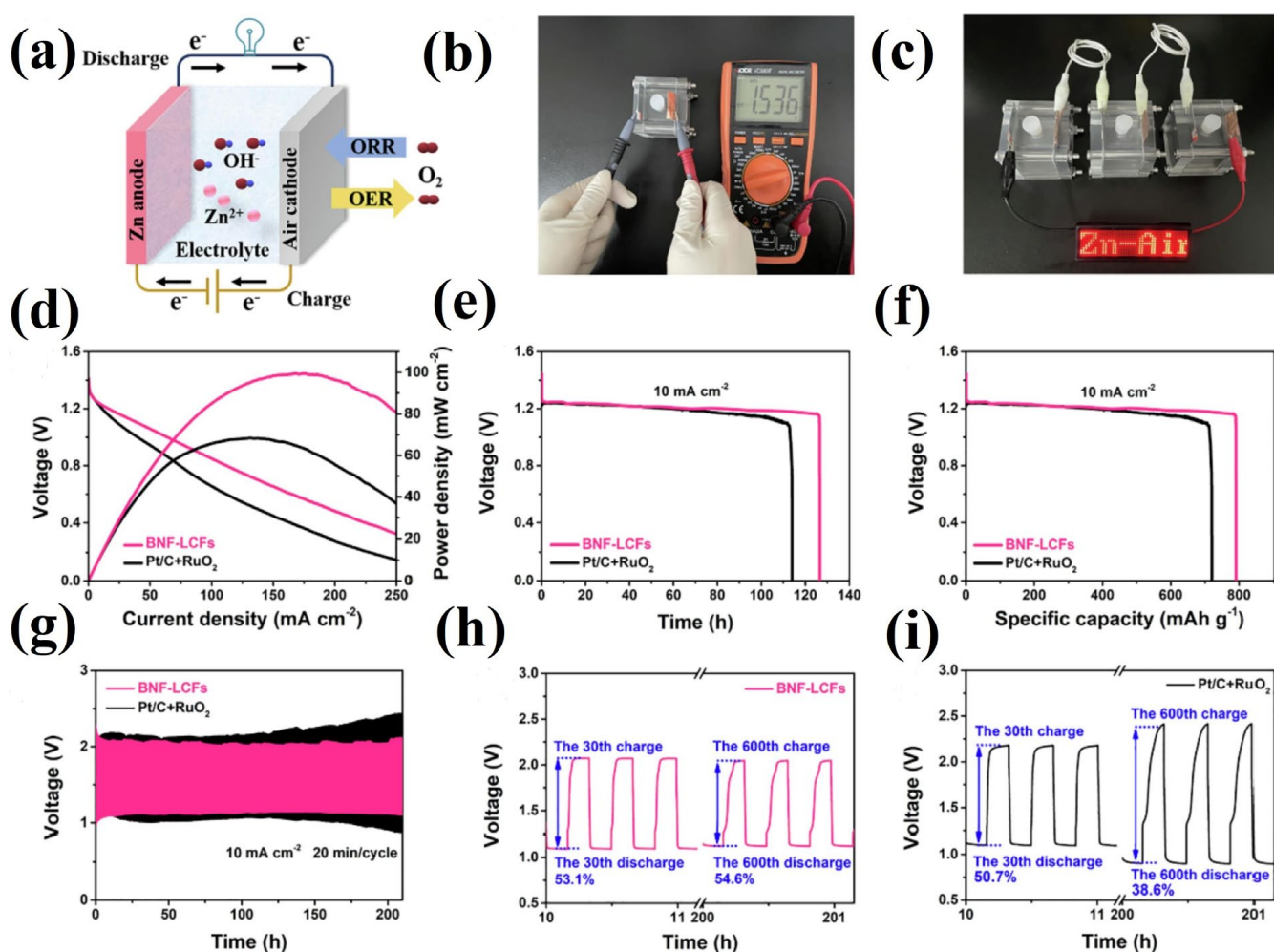


**Figure 4.** Scheme of a ZAB (a),  $E_{OCV}$  of BNF-LCF-based ZAB (b), LEDs powered by three ZABs assembled with BNF-LCFs (c), discharge polarisation curves and power density curves of ZABs assembled with BNF-LCFs or  $Pt/C + RuO_2$  (d), discharge curves of ZABs assembled with BNF-LCFs or  $Pt/C + RuO_2$  (e), specific capacities of ZABs assembled with BNF-LCFs or  $Pt/C + RuO_2$  standardised to the quality of the Zn plate consumed (f), discharge–charge cycle properties of ZABs assembled with BNF-LCFs or  $Pt/C + RuO_2$  (g–i) [59]. Copyright 2022, *Applied Surface Science*.

Porous materials doped with transition metals have been studied as ORR/OER catalysts [63]. However, metal particle agglomeration and leaching after long-term usage are still a problem to be tackled. In contrast to metal-loaded catalysts, metal-free carbon materials do not suffer from particle agglomeration or leaching and, consequently, may display better stability through long-term usage.

Quian and coworkers demonstrated that MOFs can be applied as precursors to synthesise noble-metal-free ORR/OER cathodic electrocatalysts with excellent performance in rechargeable Zn-air batteries [58]. MOF-based materials, particularly bimetallic MOFs, are known as promising electrocatalysts because of their tunable porosity, high surface area, and flexible structure/composition. Nevertheless, MOF-based materials typically have poor electrical conductivity and reduced functionality. Using MOF structures as precursors is a well-recognised method to synthesise high-performance electrocatalysts. For example, an MOF-derived  $Co_9S_8/Co-N_x/CoNi/Ni_3S_2@CNS-4$  catalyst was described to have good ORR/OER performance. A peak power density of  $206.9\ mW\ cm^{-2}$  suggested good Zn-air battery performance [64]. NiFe-MOF/NiFe<sub>2</sub>O<sub>4</sub> hollow spheres exhibited excellent ORR and OER performance, explained by the synergistic effect involving NiFe-MOF and NiFe<sub>2</sub>O<sub>4</sub> [62].

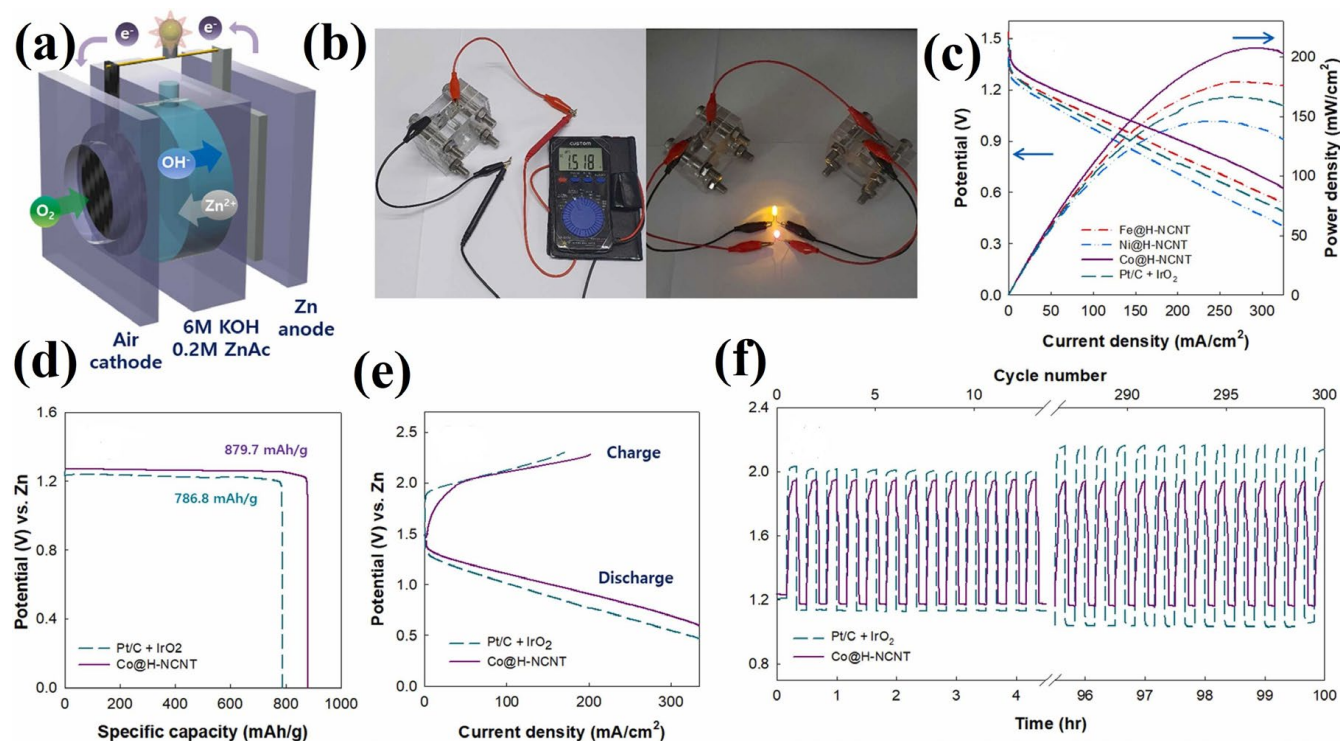


**Figure 5.** Scheme of ZAB (a),  $E_{OCV}$  and LED lit by the Co@H-NCNT-loaded ZAB (b), power density and discharge curves (c), galvanostatic discharge curves versus specific capacity (d), discharge and charge curves (e), and galvanostatic cycling response of catalyst-loaded ZABs (f) [61]. Copyright 2023, *Applied Catalysis B: Environmental*.

Electrocatalysts doped with two or more metals are also recognised to have higher catalytic activity compared to their single-metal counterparts. For instance, one-step high-temperature pyrolysis resulted in a trimetallic electrocatalyst (FeZrRu/C) with notable ORR/OER catalytic activity. A ZAB with FeZrRu/C reached a power density of ca.  $221\text{ mW cm}^{-2}$  [65].

Zhang and coworkers constructed a Co-N-C and NiFe layered double hydroxide as a composite for OER/ORR catalysis. Mn<sub>3</sub>O<sub>4</sub>-based and FeCo-based spinel oxide nanocomposites were produced by Qiu et al. for the ORR and OER, respectively. In studies by Chen et al., Fe, Co-based oxide, and their composite with N-doped graphene were prepared to reach higher ORR/OER performances. Nanoporous high-entropy spinel has recently been demonstrated to be a bifunctional ORR/OER electrocatalyst due to its tunable surface electronic structure [57]. Other types of electrocatalysts such as perovskite-type metal oxide mixed with carbon materials have been demonstrated as promising materials for MABs because of their adequate ORR/OER behaviour [66].

Several groups of exceptional ORR/OER electrocatalysts have been identified, including carbon-based electrocatalysts, transition metal nitrides, oxides, MOFs, and covalent organic frameworks. Table 4 summarises the evaluated electrocatalysts and the corresponding batteries' performance. Still, one should keep in mind that the cost of an electrocatalyst determines its potential use, along with the summarised parameters. The price of noble-metal-based electrocatalysts can be several orders of magnitude higher than that of, for instance, transition-metal-based ones.

**Table 4.** The performance of the bifunctional ORR/OER electrocatalysts and the corresponding aqueous metal–air batteries.

Bifunctional Air Cathode	$E_{OCV}$ (V) vs. RHE	$E_{1/2}$ (V) vs. RHE	$\eta_{10}$ (V) vs. RHE	Charge and Discharge Voltage (V)	Durability	$P_{max}$ (mW cm <sup>-2</sup> )	Specific Capacity (mAh g <sup>-1</sup> )	Ref.
BNPC-1100 <sup>1</sup>	/	0.793	1.38	2.19 and 1.16 V after 100 h of the test.	The ZAB did not show significant performance loss at a charge–discharge current density of 2 mA cm <sup>-2</sup> for 100 h.	/	/	[58]
BNPC-1000	/	0.749	1.41	The discharging voltage was 1.12 V after 100 h of the test.	The ZAB deteriorated during the 100 h cycling test.	//	/	[58]
BNF-LCF <sup>2</sup>	1.536	/	1.542	2.07 and 1.10 V.	The ZAB showed a stable charge–discharge performance after 600 cycles.	99.4 at ~0.57 V and ~175 mA cm <sup>-2</sup>	791.5 at 10 mA cm <sup>-2</sup>	[59]
Pt/C + RuO <sub>2</sub>	1.507	/	/	2.17 and 1.10 V.	The ZAB's charge–discharge performance rapidly dropped after the 300th cycle.	68.3 at ~0.53 V and ~130 mA cm <sup>-2</sup>	720 at 10 mA cm <sup>-2</sup>	[59]
BM_30_350_O <sub>2</sub> <sup>3</sup>	/	/	1.60	2.03 and 1.26 V.	The ZAB's efficiency reduced to 55% after 30 h.	34.6 at 0.52 V and 67.1 mA cm <sup>-2</sup>	764 at 5 mA cm <sup>-2</sup> ; 738 at 10 mA cm <sup>-2</sup>	[66]
Pt/C	/	/	/	/	The ZAB's efficiency reduced to 52% after 30 h of continuous charge–discharge cycling.	69.4 at 0.52 V and 110.1 mA cm <sup>-2</sup>	741 at 5 mA cm <sup>-2</sup> ; 737 at 10 mA cm <sup>-2</sup>	[66]
Co@H-NCNT <sup>4</sup>	1.520	/	1.544	/	The ZAB showed good cycle stability for 300 cycles (100 h).	207 at ~0.69 V and ~300 mA cm <sup>-2</sup>	879.7	[61]
Ni@H-NCNT	/	/	/	/	/	145.7 at ~0.61 V and ~240 mA cm <sup>-2</sup>		[61]
Fe@H-NCNT	/	/	/	/	/	178.8 at ~0.67 V and ~265 mA cm <sup>-2</sup>		[61]
Pt/C-IrO <sub>2</sub>	/	/	/	/	/	166.1 at ~0.64 V and ~260 mA cm <sup>-2</sup>	786.8	[61]
Co <sub>3</sub> S <sub>4</sub> @Co <sub>3</sub> O <sub>4</sub> /NSC-260-8	1.420	0.822	1.512	2.073 and 1.134 V.	The ZAB showed robust stability and no obvious decrease in the voltage for 200 h of charge–discharge cycles.	122 at 0.45 V and 272 mA cm <sup>-2</sup>	885 at 20 mA cm <sup>-2</sup>	[63]
NiFe-MOF/NiFe <sub>2</sub> O <sub>4</sub>	1.397	/	1.502	1.96 and 1.13 V.	/	158.4 at 0.64 V and 246.1 mA cm <sup>-2</sup>	700 at 2 mA cm <sup>-2</sup>	[62]
Co <sub>9</sub> S <sub>8</sub> /Co-N <sub>x</sub> /CoNi/Ni <sub>3</sub> S <sub>2</sub> @CNS-4	1.59	0.860	1.580	/	/	206.9 at 0.64 V and 325 mA cm <sup>-2</sup> ,	801 at 10 mA cm <sup>-2</sup>	[64]
FeZrRu/C	1.46	0.912	1.650	/	The ZAB showed stable discharge and charge potential for more than 10 h.	221.34 at ~0.63 V and ~350 mA cm <sup>-2</sup>	/	[65]
Fe <sub>3</sub> O <sub>4</sub> /CoO@CF	1.46	0.83	1.600		The ZAB showed long-term stability in charge/discharge performance.	137 at ~0.68 V and ~200 mA cm <sup>-2</sup>	740 at 5 mA cm <sup>-2</sup>	[60]

The overpotential ( $\eta_{10}$ ) for the OER was calculated by the following formula:  $\eta_{10}$  (V) =  $E_{RHE}$  – 1.23 V at 10 mA cm<sup>-2</sup>. BNPC <sup>1</sup>—B-N dual-doped highly porous carbon; BNF-LCFs <sup>2</sup>—B, N, and F tri-doped lignin-based carbon porous nanofibres; BM\_30\_350\_O<sub>2</sub> <sup>3</sup>—co-doped LaMnO<sub>3</sub> perovskite mixed with a carbon black material; H-NCNT <sup>4</sup>—porous N-doped carbon nanotubes.

## 6. Conclusions

This work presented the latest research and observed performances pertaining to ORR and bifunctional OER/ORR air cathodes in aqueous metal–air batteries. An overview of the latest research on developing aqueous metal–air batteries is of fundamental importance for potential practical purposes. In the last few decades, more and more research has been related to the development of OER or bifunctional OER/ORR electrocatalysts applicable in rechargeable aqueous metal–air batteries, which could be one of the main solutions for energy storage. Hence, aqueous metal–air batteries with low costs and favourable performance indicators, such as a high peak power density, high specific capacity, and good durability, are future candidates for environmentally friendly energy devices.

**Author Contributions:** Conceptualisation, J.M. and B.Š.; investigation, A.N., M.M., J.M. and B.Š.; writing—original draft preparation, A.N., M.M., J.M. and B.Š.; writing—review and editing, J.M., C.A.C.S. and B.Š.; visualisation, J.M.; supervision, J.M., B.Š. and C.A.C.S. All authors have read and agreed to the published version of the manuscript.

**Funding:** This research was funded by the Ministry of Science, Technological Development and Innovation of the Republic of Serbia (contract no. 451-03-47/2023-01/200146), as well as the Portuguese Foundation for Science and Technology (FCT, Portugal), project EXPL/EQU-EQU/0517/2021.

**Institutional Review Board Statement:** This study did not require ethical approval.

**Informed Consent Statement:** This study is not involving humans.

**Data Availability Statement:** Data are available on request.

**Conflicts of Interest:** The authors declare no conflict of interest. The funders had no role in the design of the study; in the collection, analyses, or interpretation of data; in the writing of the manuscript; or in the decision to publish the results.

## References

- Yaqoob, L.; Noor, T.; Iqbal, N. An overview of metal-air batteries, current progress, and future perspectives. *J. Energy Storage* **2022**, *56*, 106075. [[CrossRef](#)]
- Li, Y.; Lu, J. Metal-Air Batteries: Will They Be the Future Electrochemical Energy Storage Device of Choice? *ACS Energy Lett.* **2017**, *2*, 1370–1377. [[CrossRef](#)]
- Liu, Q.; Pan, Z.; Wang, E.; An, L.; Sun, G. Aqueous metal-air batteries: Fundamentals and applications. *Energy Storage Mater.* **2020**, *27*, 478–505. [[CrossRef](#)]
- Li, L.; Chang, Z.-W.; Zhang, X.B. Recent Progress on the Development of Metal-Air Batteries. *Adv. Sustain. Syst.* **2017**, *1*, 1700036r. [[CrossRef](#)]
- Chen, S.; Zhang, M.; Zou, P.; Sun, B.; Tao, S. Historical development and novel concepts on electrolytes for aqueous rechargeable batteries. *Energy Environ. Sci.* **2022**, *15*, 1805–1839. [[CrossRef](#)]
- Wang, C.; Yu, Y.; Niu, J.; Liu, Y.; Bridges, D.; Liu, X.; Pooran, J.; Zhang, Y.; Hu, A. Recent progress of metal-air batteries—A mini review. *Appl. Sci.* **2019**, *9*, 2787. [[CrossRef](#)]
- Cohn, G.; Starovetsky, D.; Hagiwara, R.; Macdonald, D.D.D.; Ein-Eli, Y. Silicon-air batteries. *Electrochim. Commun.* **2009**, *11*, 1916–1918. [[CrossRef](#)]
- Das, S.K.; Mahapatra, S.; Lahan, H. Aluminium-ion batteries: Developments and challenges. *J. Mater. Chem. A* **2017**, *5*, 6347–6367. [[CrossRef](#)]
- Dewi, E.L.; Oyaizu, K.; Nishide, H.; Tsuchida, E. Cationic polysulfonium membrane as separator in Zn-air cell. *J. Power Sources* **2003**, *115*, 149–152. [[CrossRef](#)]
- Saputra, H.; Othman, R.; Sutjipto, A.G.E.; Muhida, R. MCM-41 as a new separator material for electrochemical cell: Application in Zn-air system. *J. Memb. Sci.* **2011**, *367*, 152–157. [[CrossRef](#)]
- Gu, Z.; Xin, X.; Xu, Z.; He, J.; Wu, J.; Sun, Y.; Yao, X. Garnet Electrolyte-Based Integrated Architecture for High-Performance All-Solid-State Lithium-Oxygen Batteries. *Adv. Funct. Mater.* **2023**, *2301583*. [[CrossRef](#)]
- Liu, Z.; Zhao, N.; Zhao, X.; Wang, C.; Zhang, T.; Xu, S.; Guo, X. Combination of Li-rich layered-oxide with O<sub>2</sub> cathodes for high-energy Li-ion/Li-O<sub>2</sub> hybrid batteries. *Appl. Phys. Lett.* **2022**, *120*, 193901. [[CrossRef](#)]
- Yi, X.; Liu, X.; Qin, B.; Zhao, X.; Leong, K.W.; Pan, W.; Jiang, K.; Ma, S.; Hao, Z.; Leung, D.Y.C.; et al. High-energy composite cathode for solid-state lithium-oxygen battery boosted by ultrafine carbon nanotube catalysts and amorphous lithium peroxide. *Mater. Today Chem.* **2023**, *29*, 101430. [[CrossRef](#)]
- Tufail, M.K.; Zhai, P.; Jia, M.; Zhao, N.; Guo, X. Design of Solid Electrolytes with Fast Ion Transport: Computation-Driven and Practical Approaches. *Energy Mater. Adv.* **2023**, *4*, 1–35. [[CrossRef](#)]

15. Timofeeva, E.V.; Segre, C.U.; Pour, G.S.; Vazquez, M.; Benard, L. Aqueous air cathodes and catalysts for metal-air batteries. *Curr. Opin. Electrochem.* **2023**, *38*, 101246. [[CrossRef](#)]
16. Wang, H.; Xu, Q. Materials Design for Rechargeable Metal-Air Batteries. *Matter* **2019**, *1*, 565–595. [[CrossRef](#)]
17. Rahman, M.A.; Wang, X.; Wen, C. High Energy Density Metal-Air Batteries: A Review. *J. Electrochem. Soc.* **2013**, *160*, A1759–A1771. [[CrossRef](#)]
18. Salado, M.; Lizundia, E. Advances, challenges, and environmental impacts in metal–air battery electrolytes. *Mater. Today Energy* **2022**, *28*, 101064. [[CrossRef](#)]
19. Sun, J.; Wang, N.; Qiu, Z.; Xing, L.; Du, L. Recent Progress of Non-Noble Metal Catalysts for Oxygen Electrode in Zn-Air Batteries: A Mini Review. *Catalysts* **2022**, *12*, 843. [[CrossRef](#)]
20. Hosseini, S.; Chiu, C.Y.; Pourzolfaghar, H.; Su, C.A.; Li, Y.Y. Techno-economically feasible beverage can as superior anode in rechargeable Al-air batteries. *Sustain. Mater. Technol.* **2023**, *35*, e00560. [[CrossRef](#)]
21. Chawla, N.; Safa, M. Sodium batteries: A review on sodium-sulfur and sodium-air batteries. *Electronics* **2019**, *8*, 1201. [[CrossRef](#)]
22. Zhang, T.; Tao, Z.; Chen, J. Magnesium-air batteries: From principle to application. *Mater. Horiz.* **2014**, *1*, 196–206. [[CrossRef](#)]
23. Weinrich, H.; Durmus, Y.E.; Tempel, H.; Kungl, H.; Eichel, R.-A. Silicon and Iron as Resource-Efficient Anode Materials for Ambient-Temperature Metal-Air Batteries: A Review. *Materials* **2019**, *12*, 2134. [[CrossRef](#)] [[PubMed](#)]
24. Lee, D.U.; Xu, P.; Cano, Z.P.; Kashkooli, A.G.; Park, M.G.; Chen, Z. Recent progress and perspectives on bi-functional oxygen electrocatalysts for advanced rechargeable metal-air batteries. *J. Mater. Chem. A* **2016**, *4*, 7107–7134. [[CrossRef](#)]
25. Luo, X.; Zhao, S.; Luo, Z.; Li, S.; Zhao, X.; Fang, Q.; Wei, X.; Wang, H.; Wang, C.; Zhu, Z.; et al. Synergies of Ru/Co Nanoparticles and Co Single Atoms Active Sites toward Efficient Electrocatalysis of Oxygen Reduction Reaction for Zn-Air Battery. *Adv. Funct. Mater.* **2023**, *463*, 142184. [[CrossRef](#)]
26. Niu, W.J.; Yan, Y.Y.; Li, R.J.; Zhao, W.W.; Chen, J.L.; Liu, M.J.; Gu, B.; Liu, W.W.; Chueh, Y.L. Identifying the impact of Fe nanoparticles encapsulated by nitrogen-doped carbon to Fe single atom sites for boosting oxygen reduction reaction toward Zn-air batteries. *Chem. Eng. J.* **2023**, *456*, 140858. [[CrossRef](#)]
27. Yang, T.; Chen, Y.; Tian, M.; Liu, X.; Zhang, F.; Zhang, J.; Wang, K.; Gao, S. Engineering the electronic structure of Fe-N/C catalyst via fluorine self-doping for enhanced oxygen reduction reaction in liquid and all-solid-state Zn-air batteries. *Electrochim. Acta* **2023**, *443*, 141907. [[CrossRef](#)]
28. Li, J.; Zou, S.; Huang, J.; Wu, X.; Lu, Y.; Liu, X.; Song, B.; Dong, D. Mn-N-P doped carbon spheres as an efficient oxygen reduction catalyst for high performance Zn-Air batteries. *Chinese Chem. Lett.* **2023**, *34*, 107222. [[CrossRef](#)]
29. Wang, R.; Meng, Z.; Yan, X.; Tian, T.; Lei, M.; Pashameah, R.A.; Abo-Dief, H.M.; Algadi, H.; Huang, N.; Guo, Z.; et al. Tellurium intervened Fe-N codoped carbon for improved oxygen reduction reaction and high-performance Zn-air batteries. *J. Mater. Sci. Technol.* **2023**, *137*, 215–222. [[CrossRef](#)]
30. Park, J.; Lee, J.; Alfaruqi, M.H.; Kwak, W.-J.; Kim, J.; Hwang, J.-Y. Initial investigation and evaluation of potassium metal as an anode for rechargeable potassium batteries. *J. Mater. Chem. A* **2020**, *8*, 16718–16737. [[CrossRef](#)]
31. Vij, V.; Sultan, S.; Harzandi, A.M.; Meena, A.; Tiwari, J.N.; Lee, W.G.; Yoon, T.; Kim, K.S. Nickel-based electrocatalysts for energy-related applications: Oxygen reduction, oxygen evolution, and hydrogen evolution reactions. *ACS Catal.* **2017**, *7*, 7196–7225. [[CrossRef](#)]
32. Feng, C.; Faheem, M.B.; Fu, J.; Xiao, Y.; Li, C.; Li, Y. Fe-Based Electrocatalysts for Oxygen Evolution Reaction: Progress and Perspectives. *ACS Catal.* **2020**, *10*, 4019–4047. [[CrossRef](#)]
33. Zhao, X.; Liu, X.; Huang, B.; Wang, P.; Pei, Y. Hydroxyl group modification improves the electrocatalytic ORR and OER activity of graphene supported single and bi-metal atomic catalysts (Ni, Co, and Fe). *J. Mater. Chem. A* **2019**, *7*, 24583–24593. [[CrossRef](#)]
34. Kundu, M.K.; Mishra, R.; Bhowmik, T.; Kanrar, S.; Barman, S. Three-dimensional hierarchically porous iridium oxide-nitrogen doped carbon hybrid: An efficient bifunctional catalyst for oxygen evolution and hydrogen evolution reaction in acid. *Int. J. Hydrogen Energy* **2020**, *45*, 6036–6046. [[CrossRef](#)]
35. Milikić, J.; Stojanović, S.; Damjanović-Vasilić, L.; Vasilić, R.; Šljukić, B. Efficient bifunctional cerium-zeolite electrocatalysts for oxygen evolution and oxygen reduction reactions in alkaline media. *Synth. Met.* **2023**, *292*, 117231. [[CrossRef](#)]
36. Środa, B.; Dymerska, A.G.; Zielińska, B.; Mijowska, E. Promotion of MXene ( $Ti_3C_2Tx$ ) as a robust electrocatalyst for oxygen evolution reaction via active sites of ZIF-67—In situ mechanism investigations. *Int. J. Hydrogen Energy* **2023**, *48*, 18696–18707. [[CrossRef](#)]
37. Zhang, X.P.; Wang, H.Y.; Zheng, H.; Zhang, W.; Cao, R. O–O bond formation mechanisms during the oxygen evolution reaction over synthetic molecular catalysts. *Chin. J. Catal.* **2021**, *42*, 1253–1268. [[CrossRef](#)]
38. Xia, W.; Mahmood, A.; Liang, Z.; Zou, R.; Guo, S. Earth-Abundant Nanomaterials for Oxygen Reduction. *Angew. Chem. Int. Ed.* **2016**, *55*, 2650–2676. [[CrossRef](#)] [[PubMed](#)]
39. Liang, Y.; Li, Y.; Wang, H.; Dai, H. ChemInform Abstract: Strongly Coupled Inorganic/Nanocarbon Hybrid Materials for Advanced Electrocatalysis. *ChemInform* **2013**, *44*, 2013–2036. [[CrossRef](#)]
40. Mudassar, M.; Noor, T.; Iqbal, N. Materials Science & Engineering B Advances in MXenes synthesis and MXenes derived electrocatalysts for oxygen electrode in metal-air batteries: A review. *Mater. Sci. Eng. B* **2023**, *292*, 116400. [[CrossRef](#)]
41. Markovic, N.M.; Schmidt, T.J.; Stamenkovic, V.; Ross, P.N. Oxygen Reduction Reaction on Pt and Pt Bimetallic Surfaces: A Selective Review. *Fuel Cells* **2001**, *1*, 105–116. [[CrossRef](#)]

42. Kong, J.; Cheng, W. Recent advances in the rational design of electrocatalysts towards the oxygen reduction reaction. *Cuihua Xuebao/Chin. J. Catal.* **2017**, *38*, 951–969. [CrossRef]
43. Tu, F.D.; Wu, Z.Y.; Guo, P.; Shen, L.X.; Zhang, Z.Y.; Dai, Y.K.; Ma, M.; Liu, J.; Xu, B.; Zhang, Y.L.; et al. Fe-N-C catalysts decorated with oxygen vacancies-rich CeO<sub>x</sub> to increase oxygen reduction performance for Zn-air batteries. *J. Colloid Interface Sci.* **2023**, *637*, 10–19. [CrossRef] [PubMed]
44. Shen, M.; Hu, W.; Duan, C.; Li, J.; Ding, S.; Zhang, L.; Zhu, J.; Ni, Y. Cellulose nanofibers carbon aerogel based single-cobalt-atom catalyst for high-efficiency oxygen reduction and Zn-air battery. *J. Colloid Interface Sci.* **2023**, *629*, 778–785. [CrossRef] [PubMed]
45. Yu, A.; Long, W.; Zhu, L.; Zhao, Y.; Peng, P.; Li, F.-F. Transformation of postsynthesized F-MOF to Fe/N/F-tridoped carbon nanotubes as oxygen reduction catalysts for high power density Zn-air batteries. *Chin. Chem. Lett.* **2023**, *34*, 107860. [CrossRef]
46. Zhou, G.; Yan, X.; Zhang, T.; Wang, K.; Zhang, J.; Guo, J. MOFs-derived hierarchical porous carbon supported Co@NC nanocapsules for pH universal oxygen reduction reaction and Zn-air batteries. *Appl. Surf. Sci.* **2023**, *621*, 156906. [CrossRef]
47. Cheng, C.; Sun, Z.; Li, B.; Li, Y.; Jin, C.; Xiang, T.; Wang, W.; Wu, Z.; Xue, H.; Cao, Y.; et al. Unveiling the inter-molecular charge transfer mechanism of N-doped graphene/carbon nanotubes heterostructure toward oxygen reduction process for Zn-air battery. *Appl. Surf. Sci.* **2023**, *614*, 156096. [CrossRef]
48. Chang, H.; Guo, Y.-F.; Liu, X.; Wang, P.-F.; Xie, Y.; Yi, T.-F. Dual MOF-derived Fe/N/P-tridoped carbon nanotube as high-performance oxygen reduction catalysts for Zn-air batteries. *Appl. Catal. B Environ.* **2023**, *327*, 122469. [CrossRef]
49. Zhang, Y.; He, Q.; Chen, Z.; Chi, Y.; Sun, J.; Yuan, D.; Zhang, L. Hierarchically porous Co@N-doped carbon fiber assembled by MOF-derived hollow polyhedrons enables effective electronic/mass transport: An advanced 1D oxygen reduction catalyst for Zn-air battery. *J. Energy Chem.* **2023**, *76*, 117–126. [CrossRef]
50. Zhao, Q.; Tan, X.; Liu, T.; Hou, S.; Ni, W.; Huang, H.; Zhang, J.; Yang, Z.; Li, D.; Hu, H.; et al. Engineering adjacent N, P and S active sites on hierarchical porous carbon nanoshells for superior oxygen reduction reaction and rechargeable Zn-air batteries. *J. Colloid Interface Sci.* **2023**, *633*, 1022–1032. [CrossRef]
51. Liu, Y.; Sun, Q.; Li, W.; Adair, K.R.; Li, J.; Sun, X. A comprehensive review on recent progress in aluminum–air batteries. *Green Energy Environ.* **2017**, *2*, 246–277. [CrossRef]
52. Cheng, R.; Li, K.; Li, Z.; Jiang, M.; Wang, F.; Yang, Z.; Zhao, T.; Meng, P.; Fu, C. Rational design of boron-nitrogen coordinated active sites towards oxygen reduction reaction in aluminum-air batteries with robust integrated air cathode. *J. Power Sources* **2023**, *556*, 232476. [CrossRef]
53. Jeong, S.; Kim, S.; Son, H.; Li, O.L. Plasma-engineered cobalt nanoparticle encapsulated N-doped graphene nanoplatelets as high-performance oxygen reduction reaction electrocatalysts for aluminum–air batteries. *Catal. Today* **2023**, *420*, 114025. [CrossRef]
54. Wang, Y.; Li, K.; Cheng, R.; Xue, Q.; Wang, F.; Yang, Z.; Meng, P.; Jiang, M.; Zhang, J.; Fu, C. Enhanced electronic interaction between iron phthalocyanine and cobalt single atoms promoting oxygen reduction in alkaline and neutral aluminum-air batteries. *Chem. Eng. J.* **2022**, *450*, 138213. [CrossRef]
55. Wang, Q.; Xu, X.; Lu, D. Synthesis of cobalt-anchored N-doped carbon as an oxygen reduction reaction catalyst for aluminum-air batteries. *Appl. Catal. A Gen.* **2022**, *646*, 118847. [CrossRef]
56. Tang, W.; Li, B.; Teng, K.; Wang, X.; Liu, R.; Wu, M.; Zhang, L.; Ren, P.; Zhang, J.; Feng, M. Advanced noble-metal-free bifunctional electrocatalysts for metal-air batteries. *J. Mater.* **2022**, *8*, 454–474. [CrossRef]
57. Yu, T.; Xu, H.; Jin, Z.; Zhang, Y.; Qiu, H.J. Noble metal-free high-entropy oxide/Co-N-C bifunctional electrocatalyst enables highly reversible and durable Zn-air batteries. *Appl. Surf. Sci.* **2023**, *610*, 155624. [CrossRef]
58. Qian, Y.; Hu, Z.; Ge, X.; Yang, S.; Peng, Y.; Kang, Z.; Liu, Z.; Lee, J.Y.; Zhao, D. A metal-free ORR/OER bifunctional electrocatalyst derived from metal-organic frameworks for rechargeable Zn-Air batteries. *Carbon* **2017**, *111*, 641–650. [CrossRef]
59. Wang, Y.; Gan, R.; Zhao, S.; Ma, W.; Zhang, X.; Song, Y.; Ma, C.; Shi, J. B, N, F tri-doped lignin-derived carbon nanofibers as an efficient metal-free bifunctional electrocatalyst for ORR and OER in rechargeable liquid/solid-state Zn-air batteries. *Appl. Surf. Sci.* **2022**, *598*, 153891. [CrossRef]
60. Li, X.; Liu, Y.; Xu, H.; Zhou, Y.; Chen, X.; An, Z.; Chen, Y.; Chen, P. Tuning active sites for highly efficient bifunctional oxygen electrocatalysts of rechargeable Zn-air battery. *J. Colloid Interface Sci.* **2023**, *640*, 549–557. [CrossRef]
61. Choi, E.Y.; Kim, D.E.; Lee, S.Y.; Park, C.B.; Kim, C.K. Cobalt nanoparticles-encapsulated holey nitrogen-doped carbon nanotubes for stable and efficient oxygen reduction and evolution reactions in rechargeable Zn-air batteries. *Appl. Catal. B Environ.* **2023**, *325*, 122386. [CrossRef]
62. Lan, T.; Du, H.; Li, Y.; Qu, K.; Zhao, J.; Zhang, X.; Dong, Y.; Zhang, Y.; Zhang, X.; Zhang, D. One-pot synthesis of NiFe-MOF/NiFe<sub>2</sub>O<sub>4</sub> hollow spheres and their application as bifunctional ORR/OER electrocatalysts in Zn-air batteries. *J. Alloys Compd.* **2023**, *943*, 169144. [CrossRef]
63. Bo, L.; Shi, W.; Nian, F.; Hu, Y.; Pu, L.; Li, P.; Zhang, Z.; Tong, J. Interface engineering of Co<sub>3</sub>S<sub>4</sub>@Co<sub>3</sub>O<sub>4</sub>/N, S-doped carbon core@shell nanostructures serve as an excellent bifunctional ORR/OER electrocatalyst for rechargeable Zn-air battery. *Sep. Purif. Technol.* **2023**, *307*, 122536. [CrossRef]
64. Gopalakrishnan, M.; Etesami, M.; Theerthagiri, J.; Choi, M.Y.; Wannapaiboon, S.; Nguyen, M.T.; Yonezawa, T.; Kheawhom, S. Tailoring the MOF structure via ligand optimisation afforded a dandelion flower like CoS/Co-Nx/CoNi/NiS catalyst to enhance the ORR/OER in Zn-air batteries. *Nanoscale* **2022**, *14*, 17908–17920. [CrossRef]

65. Zhang, Y.; Wang, Z.; Guo, S.; Zhang, Z.; Zeng, X.; Dong, P.; Li, M.; Xiao, J.; Zhang, C.; Hu, J.; et al. FeZrRu Trimetallic bifunctional oxygen electrocatalysts for rechargeable Zn-air batteries. *Electrochim. Acta* **2023**, *437*, 141502. [[CrossRef](#)]
66. García-Rodríguez, M.; Flores-Lasluisa, J.X.; Cazorla-Amorós, D.; Morallón, E. Metal oxide Perovskite-Carbon composites as electrocatalysts for Zn-air batteries. Optimisation of ball-milling mixing parameters. *J. Colloid Interface Sci.* **2023**, *630*, 269–280. [[CrossRef](#)] [[PubMed](#)]

**Disclaimer/Publisher's Note:** The statements, opinions and data contained in all publications are solely those of the individual author(s) and contributor(s) and not of MDPI and/or the editor(s). MDPI and/or the editor(s) disclaim responsibility for any injury to people or property resulting from any ideas, methods, instructions or products referred to in the content.